Chromosomal instability can favor macrophage-mediated immune response and induce a broad, vaccination-like anti-tumor IgG response

Brandon H. Hayes[1-3], Mai Wang[1,2], Hui Zhu[1,2], Steven H. Phan[1,2], Jason C. Andrechak[1-3], Alexander H. Chang[1,2], Lawrence J. Dooling[1,2], Michael P. Tobin[1-3], Tristan Marchena[1,2], Dennis E. Discher[1-3,†]

[1]Molecular and Cell Biophysics Lab, [2]Physical Sciences Oncology Center at Penn, [3]Bioengineering Graduate Group, University of Pennsylvania, Philadelphia, PA, USA.
†Correspondence: discher@seas.upenn.edu

Abstract

Chromosomal instability (CIN), a state in which cells undergo mitotic aberrations that generate chromosome copy number variations, generates aneuploidy and is thought to drive cancer evolution. Although associated with poor prognosis and reduced immune response, CIN generates aneuploidy-induced stresses that could be exploited for immunotherapies. Macrophages, particularly, have been understudied in the CIN context. Here, through MPS1 inhibition-induced CIN in poorly immunogenic B16F10 mouse melanoma, we find that CIN-afflicted cancer cells skew macrophages towards an anti-cancer phenotype while also pushing them away from a pro-cancer one. We confirm these findings via RNA-sequencing, protein expression, and short-term tumor studies. These results further translate to *in vivo* efficacy in suppressing tumor growth: Mice can survive challenges of CIN-afflicted tumors. Long-term survival, however, is dependent on CD47 expression and IgG opsonization. Mice bearing CIN-afflicted tumors with wild-type CD47 levels see prolonged survival compared to their chromosomally stable counterparts, but all succumb. Mice bearing CIN-afflicted CD47 knockout tumors, however, show 28% long-term survival. When CD47 knockout was further paired with IgG opsonization, survival rate increased to 97%. Successful rejection and clearance of CIN-afflicted tumors induced *de novo* anti-cancer IgG antibodies that were multi-epitope and functionally promoted macrophage-mediated phagocytosis. These *de novo* IgG antibodies could also suppress *in vitro* tumoroid and *in vivo* tumor growth in a CD47 knockout context. These results highlight an unexpected therapeutic benefit from CIN when paired with maximal macrophage anti-cancer activity: an anti-cancer vaccination-like antibody response that can lead to durable cures and further potentiate cell-mediated acquired immunity.

(250 words; 250 max)

Keywords: macrophages, aneuploidy, phagocytosis, CD47, antibodies

34 **Introduction**

35 Chromosomal instability (CIN) has long been thought to be indicative of poor prognosis and
36 reduced immune cell activity against tumors (Davoli et al., 2017; Vasudevan et al., 2021). CIN
37 is a state of high frequency of chromosome mis-segregation, which often generates micronuclei
38 and can ultimately cause aneuploidy—an abnormal number of chromosomes. CIN-induced
39 genomic heterogeneity can serve as a tumor promotor (Sheltzer et al., 2017) and allow some
40 tumor subpopulations to favor aggression, metastatic potential, immune evasion, and resistance
41 to therapies (Ben-David & Amon, 2019; Chunduri & Storchová, 2019; Vasudevan et al., 2021).
42 However, early-stage CIN also induces anti-cancer vulnerabilities (Cohen-Sharir et al., 2021;
43 Vasudevan et al., 2020), such as proliferation deficits (Wang et al., 2021). These early-stage
44 CIN-afflicted cells have yet to adapt and achieve aneuploidies that favor growth and immune
45 evasion (Tripathi et al., 2019, Vasudevan et al., 2021). CIN in diploid cells that is caused by
46 spindle checkpoint disruption by MPS1 inhibition (MPS1i) further induces a senescence-
47 associated secretory pathway phenotype and upregulation of NF-κB and interferon-mediated
48 pathways, among others, that drive immune clearance of chromosomally aberrant cells
49 (Santaguida et al., 2017; Wang et al., 2021). CIN and ploidy changes also inhibit tumor growth
50 in immunocompetent mice while having little effect in immunocompromised mice (Senovilla et
51 al., 2012; Boilève et al., 2013), suggesting CIN can somehow increase immunogenicity.
52
53 Recent analyses of The Cancer Genome Atlas (TCGA) particularly showed that highly aneuploid
54 tumors have macrophages that are polarized toward a pro-cancer, M2-like phenotype, among
55 other pro-cancer immune changes (Davoli et al., 2017; Taylor et al., 2018). MPS1i-treated
56 cancer cells have also been occasionally found to escape immune-mediated clearance (Wang
57 et al., 2021), but another study further found that cancer cells respond to CIN ultimately by
58 triggering IL-6-STAT3 signaling (Hong et al., 2022) that protect from CIN-induced cell death,
59 minimize interferon-related anti-cancer responses, and allow cells to adapt to CIN- and
60 aneuploidy-induced stresses. Among these studies, two key observations stood out. First, ploidy
61 changes tend to increase factors that can promote macrophage-mediated phagocytosis (Chao
62 et al., 2010; Krysko et al., 2018). Second, pro-survival signaling amidst CIN leads to an increase
63 of other factors (such as IL6) that induce a pro-cancer, M2-like phenotype (Fernando et al.,

2014). Together, these observations led us to hypothesize that macrophages may play a key effector role in confronting and influencing CIN- and aneuploidy-afflicted tumors.

Macrophages have become attractive candidates for immunotherapies due to their ability to phagocytose cancer cells (Alvey et al., 2018; Klichinsky et al., 2020). Generally, phagocytosis of 'self' cells is inhibited by the key macrophage checkpoint interaction between SIRPα on the macrophage and CD47 on the target cell (Oldenborg et al., 2000). CD47 is ubiquitously expressed on all cells, including cancer cells (Willingham et al., 2012). While tumor cell engulfment can be driven to some extent via IgG opsonization by using anti-tumor monoclonal antibodies that bind Fc receptors on macrophages (Alvey et al., 2017; Morrissey et al., 2020; Suter et al., 2021; Tsai & Discher, 2008), this is generally insufficient to eliminate cancers, especially solid tumors. Maximal macrophage-mediated phagocytosis is achieved when CD47-SIRPα signaling is disrupted, in addition to IgG opsonization. However, achieving complete tumor rejection is still a major challenge for macrophage-oriented therapies (Ingram et al., 2017; Sockolosky et al., 2016), even after having identified these three key factors. Previous studies achieved durable cures in immunocompetent mice, with some acquired immunity benefits, but tumor rejection success is highly variable (Dooling et al., 2022; Hayes et al., 2022). Additionally, *in vivo* macrophages often polarize toward tumor-associated macrophage (TAM) phenotypes, which correlate with poor clinical prognoses (Cerezo-Wallis et al., 2020; Noy & Pollard, 2014). TAMs also have poor phagocytic function and promote tumor growth and invasion (Alvey et al., 2017; Georgouli et al., 2019). Nonetheless, CIN could create conditions in which macrophages are not outcompeted in number by cancer cell proliferation and avoid becoming TAM-like.

Inspired by recent advances in exploiting CIN-related anti-cancer vulnerabilities, we hypothesized that early-stage CIN in cancer cells may stimulate higher anti-cancer macrophage activity than their chromosomally stable counterparts (under conditions of maximal phagocytosis). Our results provide detailed *in vitro* and *in vivo* evidence that early-stage CIN in cancer favors anti-cancer macrophage activity and consistently leads to durable cures in mice when under conditions of maximal phagocytosis. Elimination of these CIN-afflicted solid tumors further drives development of both anti-cancer opsonizing IgGs and enhanced cell-mediated immunity, both of which help suppress growth against aggressive chromosomally stable tumors.

Results

MPS1i-induces CIN and generates conditions that favor anti-cancer macrophages while minimizing skewing towards a pro-cancer macrophage phenotype

To investigate the possible effects that CIN may have in mediating macrophage immune response, we chose to work with the poorly immunogenic B16F10 mouse melanoma model. To induce CIN in B16F10, we treated cells with the MPS1 inhibitor reversine (Hong et al., 2022; Kitajiam et al., 2022; Santaguida et al., 2010; Santaguida et al., 2017). Treatment occurred for 24 h, after which the drug was washed out, and cells were allowed to recover for an additional 48 h (**Fig. 1A**). After the recovery period, we quantified CIN in B16F10 cells, characterized its effects in early-stage tumors, and studied potential effects on macrophages *in vitro* (**Fig. 1A**). We first confirmed that MPS1i treatment increased the frequency of micronuclei formation in interphase cells (**Fig. 1B**), as micronuclei are often used as a surrogate for CIN and genome instability (Cohen-Sharier et al., 2020; Crasta et al., 2012; Harding et al., 2017; Mackenzie et al., 2017). Regardless of the MPS1i concentration used, we saw substantial increases over the cell line's baseline level of micronuclei formation. We further verified these results with other MPS1i inhibitors AZ3146 and BAY 12-17389 (**Fig. S1A**) to confirm the effect was not somehow limited to just reversine. Upon confirmation of increased micronuclei induction, we then proceeded to quantitatively confirm and assess copy number variations that resulted from MPS1i treatment using single-cell RNA-sequencing. For DMSO-treated B16F10 cells, approximately 10% of the population were considered aneuploid outliers (**Fig. 1C-top; S1B-C**) – cells with copy number profiles that are 2.5 standard deviations away from the distribution peak (see **Methods**). However, 34% of the MPS1i-treated B16F10 cells were aneuploid (**Fig. 1C-bottom; S1B-C**).

After confirming that MPS1i indeed induces CIN and quantifiable aneuploidy in B16F10 cells, we next sought to understand how CIN may affect early-stage immune response and tumor development. We proceeded to establish tumors in mice with either MPS1i-treated or DMSO-treated B16F10 (following the same schema outlined in **Fig. 1A**). We isolated tumors from mice at two timepoints, five and ten days after initial challenge, and then we processed whole-tumors for bulk RNA-sequencing (**Fig. 1D**). Comparison of tumors comprised of MPS1i-treated and DMSO-treated cells by differential gene expression showed distinct downregulated transcripts

126 for numerous genes encoding M2-like (pro-cancer) macrophage polarization markers (**Fig. 1E**).
127 At day 5 post-challenge, we see that classical M2-like, pro-cancer markers *Arg1*, *Marco*, and
128 *Cd274* are downregulated. However, several M2 markers are upregulated at this timepoint:
129 *Mrc1*, *Cd163*, and genes related to the complement component 1a (C1q). By day 10, *Marco*,
130 *Mrc1*, *Cd163, Cd274,* and the C1q complex genes are now all downregulated. *Arg1*, however,
131 returns to either basal or increased expression on day 10. Overall, though, we generally see
132 globally decreased expression for most markers by day 10. Furthermore, cytokines *Ccl2*, *Ccl4*,
133 *Ccl7*, *Ccl22*, and *Il21r*, which associated with an M2-like, pro-cancer macrophage phenotype
134 (Cerezo-Wallis et al., 2020), were found to be consistently downregulated at both days 5 and 10
135 post-challenge. Gene set enrichment analysis further revealed that numerous pathways related
136 cell cycle and proliferation were also downregulated (**Fig. 1F**), consistent with previous studies
137 (Cohen-Sharir et al., 2020; Wang et al., 2021). These downregulated pathways suggest longer
138 tumor doubling time since cells have yet to adapt to these CIN-associated proliferation deficits.
139
140 The identification of downregulated M2-like macrophage markers in CIN-afflicted tumors next
141 led us to better assess how early-stage CIN in cancer may influence macrophages specifically.
142 Previous studies (Cerezo-Wallis et al., 2020; Xian et al., 2021) have found that the secretome
143 can have profound and rapid polarization effects on bone marrow-derived macrophages
144 (BMDMs) *in vitro*. We proceeded to perform a similar secretome study, in which conditioned
145 media from MPS1i-treated or DMSO-treated B16F10 cells was collected and added to previously
146 differentiated BMDMs. BMDMs were treated with conditioned media for 24 h, after which they
147 were collected and processed for single-cell RNA-sequencing (**Fig. 1G**). Unsupervised
148 clustering analysis using uniform manifold approximation and projection (UMAP) nonlinear
149 dimensionality reduction identified four distinct macrophage population clusters: two clusters (0
150 and 2) that consisted of approximately 75% of macrophages treated with MPS1i-treated B16F10
151 secretome and two clusters (1 and 3) that consisted of approximately 75% macrophages treated
152 with DMSO-treated B16F10 secretome (**Fig. 1H**).
153
154 The gene expression profiles of these clusters showed that the two clusters (1 and 3) that
155 consisted mostly of macrophages treated with DMSO-treated B16F10 secretome had increased
156 expression of anti-inflammatory, M2-like pro-cancer macrophage polarization markers (**Fig. 1I**).

157 Consistent with the whole-tumor bulk RNA-seq, we were successfully able to capture increased
158 expression of *Mrc1* in both clusters 1 and 3 and observed increased expression of *Ccl2*, *Ccl4*,
159 and *Ccl7* in cluster 3. More importantly though, gene expression revealed that clusters 1 and 3
160 tended to downregulate many genes associated with a pro-inflammatory, M1-like anti-cancer
161 response (**Fig. 1J**). Clusters 0 and 2, on the other hand, which consisted mostly of MPS1i-treated
162 B16F10 secretome, showed little-to-no expression for most M2-like, pro-cancer markers (**Fig.**
163 **1I**) and increased expression of pro-inflammatory, anti-cancer markers (**Fig. 1J**). These results
164 suggest that early-stage CIN in cancer cells engages pro-inflammatory macrophage activity.
165

166 **Macrophages polarize to an M1-like phenotype and can clear CIN-afflicted tumoroids**

167 Next, we sought to experimentally confirm the polarization effects. Here, we use B16F10 CD47
168 knockout (KO) cells (**Fig. S2A**) to remove the inhibitory effects of CD47 on phagocytosis and
169 more easily study macrophage engulfment ability (**Fig. S2B-C**). Moving forward, we chose to
170 use a B16F10 tumoroid model to better simulate the biophysical properties of the 3D tumor
171 microenvironment and proliferative capacity of tumor masses (**Fig. 2A**) (Dooling et al., 2022).
172 We chose this model primarily because 2D phagocytosis assays fail to consider the mechanical
173 cohesive forces between tumor cells and other biophysical aspects that can affect immune
174 response (Nia et al., 2020). We have previously found that macrophages need to phagocytose
175 cooperatively—large numbers of macrophages working together to overcome the mechanical
176 strength of cohesion between solid tumor cells—to achieve durables responses (Dooling et al.,
177 2022). CIN can also often induce additional effects on cells in its early stages, such as increases
178 in cell size due to cytokinesis defects and poly-aneuploidy (Chunduri & Storchová, 2019; Mallin
179 et al., 2022). Single macrophages may struggle to phagocytose these large targets in a
180 conventional 2D assay (Champion et al., 2006), even with IgG opsonization, which we
181 experimentally confirmed with MPS1i-treated cells (**Fig. S2B**). MPS1i treatment, in fact,
182 increases cell size, as measured by flow cytometry (**Fig. S2C**), although size effects are
183 confounded by decreased Tyrp1 expression, the antigen targetable for opsonization using anti-
184 Tyrp1 (**Fig. S2D**). CD47 levels were relatively consistent across treatment conditions and similar
185 to non-perturbed levels (**Fig. S2E**) for B16F10 sgCtrl. We thus hypothesized that cooperative
186 phagocytosis (Dooling et al., 2022) may be able to overcome the CIN-induced size increases
187 and reduced binding of anti-Tyrp1. BMDMs were added to pre-assembled tumoroids at a 3:1

188 ratio, and this “immuno-tumoroid” co-culture was maintained for five days. We first assessed
189 surface protein expression of macrophage polarization markers. Consistent with the polarization
190 trends in our whole-tumor bulk RNA-sequencing and single-cell RNA-sequencing of BMDMs
191 (**Fig. 1E, 1I-J**), we find that BMDMs co-cultured in tumoroids of MPS1i-treated B16F10 showed
192 increased expression of M1-like, anti-cancer macrophage markers MHCII and CD86 while
193 having decreased expression of M2-like, pro-cancer markers CD163 and CD206 (**Fig. 2B-C**).
194
195 We next wondered if these polarization studies translated to functional effects on macrophage-
196 mediated phagocytosis and clearance of tumoroids. We again prepared tumoroids, later adding
197 BMDMs to these pre-assembled tumoroids at a 3:1 ratio with either anti-Tyrp1 or mouse IgG2a
198 isotype control for IgG opsonization. In our 3D tumoroid *in vitro assays*, we found that
199 macrophages can suppress the growth of chromosomally unstable tumoroids and clear them,
200 surprisingly both with and without anti-Tyrp1 (**Fig. 2D-E**), regardless of MPS1i concentration
201 used for treatment. In contrast, DMSO-treated B16F10 cells (chromosomally stable with regular
202 proliferative capacity) require anti-Tyrp1 for macrophages to clear them (**Fig. 2D, S3B**). These
203 results link the phenotypic studies with functional effects: CIN can induce anti-cancer
204 macrophage phenotypes to favor macrophage-mediated clearance.
205
206 We also attempted to use two other MPS1i inhibitors to see if we achieved similar results:
207 tumoroids made of AZ3146-treated cells, which BMDMs could only suppress at very high
208 concentrations (**Fig. S3C-i**), and tumoroids made of BAY 12-17389-treated cells, which were
209 heavily suppressed and/or cleared similarly to tumoroids comprised of reversine-treated cells
210 (**Fig. S3C-ii**). Given that AZ3146-treated cells tended to proliferate well, we next sought to verify
211 if tumoroids made of cells treated with either BAY 12-17389 or reversine would eventually grow.
212 We observed that tumoroids decreased in size 24 h after plating, most likely due to some cell
213 death (**Fig. S3D**). Afterwards though, tumoroids generally showed some proliferation, albeit with
214 deficits. This suggests that the anti-cancer macrophage activity observed may require CIN be
215 severe enough to induce some proliferation deficits. Otherwise, low-level CIN may be tolerable
216 for cancer cells, eventually favor their evolution (Vasudevan et al., 2020), and allow cancer cells
217 to still proliferate more rapidly than phagocytosis kinetics can manage.
218

219 Lastly, we sought to confirm both our transcriptomic analyses and tumoroid surface marker
220 expression before proceeding to long-term *in vivo* experimentation. We proceeded to establish
221 tumors in mice with either MPS1i-treated or DMSO-treated B16F10 cells (the drug treatment
222 followed the same schema outlined in **Fig. 1A**). We then isolated tumors five days post-challenge
223 for immune infiltrate analyses by flow cytometry (**Fig. 2F, S5**). We found that CIN-afflicted tumors
224 had approximately 3-fold more CD45+ immune cells (**Fig. 2G-i**), 2.5-fold more CD45+ CD11b+
225 (myeloid) cells (**Fig. 2G-ii**), and a near 6-fold increase in F4/80-positive macrophage (**Fig. 2G-**
226 **iii**) compared to their DMSO counterparts. Furthermore, we found that CIN-afflicted tumors
227 showed approximately 6-fold more $CD86^{hi}$ $CD206^{lo}$ (M1-like, anti-cancer) macrophages
228 compared to their DMSO counterparts. We should note that these tumors also saw an increase
229 in $CD86^{lo}$ $CD206^{hi}$ (M2-like, pro-cancer) macrophages compared to DMSO control (**Fig. 2G-iv**).,
230 but this increase is expected given that there are generally more macrophages infiltrating these
231 tumors. Despite the increase in M2-like macrophages, these tumors made of MPS1i-treated cells
232 still have roughly 2-fold more M1-like macrophages (**Fig. 2G-iv**). These results suggest that
233 although other immune cell types infiltrate tumors, which is consistent with upregulated surface
234 expression of H2-K^b (**Fig. S4**), macrophage functional activity is indeed positively affected by
235 CIN-afflicted cancer cells.
236

237 **MPS1i-induced CIN favors tumor rejection with IgG opsonization and CD47 disruption**

238 While previous studies show that complete CD47 ablation can favor suppression and even
239 complete rejection of IgG-opsonized B16F10 tumors (Andrechak et al., 2022; Dooling et al.,
240 2022; Hayes et al., 2022; Kamber et al., 2021), inter-experimental variation is high, particularly
241 regarding complete tumor rejection and clearance. Furthermore, how CIN could influence these
242 results is unknown. Therefore, we sought to assess if CIN in B16F10, which thus far has shown
243 to skew macrophages toward an anti-cancer phenotype and away from pro-cancer one, can
244 translate to improved efficacy and consistency in macrophage-oriented therapies. For these
245 subsequent *in vivo* experiments, we first pre-treated B16F10 cells with either MPS1i or DMSO
246 for 24 h, washed the drug out, and then allowed the cells to recover for an additional 48 h (**Fig.**
247 **3A**). After the recovery period elapsed, we established tumors in mice, with either MPS1i-treated
248 or DMSO-treated B16F10 cells. To further test for CD47-mediated effects, we used either

B16F10 CD47 KO or B16F10 sgCtrl, expressing wild-type CD47 (WT) levels. Starting four days post-challenge, mice received either anti-Tyrp1 or mIgG2a isotype control for opsonization.

As expected, all tumors comprised of DMSO-treated B16F10 sgCtrl showed exponential growth and no survivors (**Fig. 3B**), consistent with previous studies (Dooling et al., 2022; Hayes et al., 2022). These results re-confirm the inhibitory effect that CD47 has on macrophage-mediated immunity (Ingram et al., 2017; Sockolosky et al., 2016; Willingham et al., 2012), suppressing macrophage immune response even with anti-Tyrp1 IgG opsonization. Mice with CIN-afflicted B16F10 sgCtrl tumors ultimately showed exponential growth and no survivors as well, but they did show increased median survival. Furthermore, median survival increased even further when mice were treated with anti-Tyrp1, such that all mice were considered partial responders (survival of 20+ days, one week longer than median survival of tumors comprised of DMSO-treated B16F10 sgCtrl without anti-Tyrp1 treatment). All tumors comprised of DMSO-treated B16F10 CD47 KO showed exponential growth and no survivors (**Fig. 3C**), regardless of anti-Tyrp1 treatment or not. However, CIN-afflicted B16F10 CD47 KO tumors showed more positive outcomes. Even without anti-Tyrp1, all challenged mice with CIN-afflicted CD47 KO tumors were either cured completely (28%) or considered partial responders. When paired with anti-Tyrp1 treatment, 97% of mice challenged with CIN-afflicted CD47 KO tumors survive.

Long-term survival results show that challenging mice with both MPS1i-treated and DMSO-treated B16F10 sgCtrl failed to yield any survivors, regardless of anti-Tyrp1 opsonization or not (**Fig. 3D-i**). Similarly, we also failed to generate any survivors among mice challenged with DMSO-treated B16F10 CD47 KO cells, regardless of anti-Tyrp1 opsonization or not (**Fig. 3D-ii**). This again highlights a challenge in optimizing macrophage-mediated therapies: achieving consistency in long-term therapeutic outcomes. Mice challenged with MPS1i-treated B16F10 CD47 KO cells, however, were able to survive, both without anti-Tyrp1 (28% survival) and with anti-Tyrp1 (97% survival) (**Fig. 3D-ii**). To determine if the degree of CIN affected survival, we also challenged mice with B16F10 CD47 KO cells treated with varying concentrations of reversine. Regardless of MPS1i concentration, >80% of mice survive when also treated with anti-Tyrp1 (**Fig. S6**). These results show that, in physiologically relevant microenvironments, early-stage CIN can favor survival when paired with IgG opsonization and CD47 disruption. This

280 further suggests that macrophages are key effector cells in achieving survival against CIN-
281 afflicted tumors, since 97% survival was achieved under conditions of maximal phagocytosis.
282
283 Although no mice challenged with CIN-afflicted B16F10 sgCtrl survived, MPS1i increase median
284 survival significantly when paired with anti-Tyrp1 opsonization (**Fig. 3D-i**). This suggests that
285 macrophages still display some anti-cancer activity, despite the inhibitory effects of CD47, and
286 are important effector cells in final therapeutic outcome. To better support the hypothesis that
287 macrophages are indeed key effector cells in rejecting CIN-afflicted tumors, we established
288 tumors comprised of wild-type (WT) B16F10 in mice. Although WT tumors are generally
289 unaffected by anti-CD47 and anti-Tyrp1 (Dooling et al., 2022; Hayes et al., 2022), we
290 hypothesized that we could eliminate CIN-afflicted WT B16F10 tumors by providing adoptive
291 transfer of marrow to increase macrophage numbers to compensate for the CD47-mediated
292 inhibition of endogenous macrophages. Furthermore, we engineered marrow by priming Fcγ
293 receptors with anti-Tyrp1, initially inhibiting CD47-SIRPα interaction via anti-SIRPα antibody
294 blockade or combining both (**Fig. 3E-i**). As expected, mice challenged with CIN-afflicted WT
295 tumors and treated with regular, unprimed marrow only had ~14% survival (**Fig. 3E-ii & iii**). This
296 result, however, was identical to chromosomally stable WT tumors treated with marrow primed
297 with both anti-SIRPα and anti-Tyrp1. These results suggest increased macrophages numbers
298 do provide some minor benefit. As the marrow engineering becomes more rigorous to maximize
299 phagocytosis, survival improves. 37% of mice challenged with CIN-afflicted WT tumors survived
300 when treated with marrow that was initially engineered with anti-SIRPα. 50% survived with
301 marrow primed with anti-Tyrp1. Lastly, 80% survived with anti-Tyrp1-primed and anti-SIRPα-
302 blocked monocytes (**Fig. 3E-ii & iii**). Altogether, these results support three conclusions: (1) the
303 increase in survival attributed to anti-SIRPα supports the idea that CD47 modulates therapeutic
304 outcome even during CIN; (2) the increase in survival attributed to anti-Tyrp1 highlights the
305 importance of IgG opsonization; (3) the high success from the combination emphasizes
306 macrophages playing a key role in achieving complete rejection and clearance.
307
308 **Clearance of CIN-afflicted tumors promotes *de novo* pro-phagocytic & anti-cancer IgG**
309 Macrophages and related phagocytic cells make up innate immunity, a first line of defense
310 against pathogens and disease, but they are also responsible for initiating acquired immunity.

311 The activation of the acquired immune response involves two branches of immunity: humoral
312 (mediated by macromolecules such as antibodies) and cell-mediated immunity (involving T cells,
313 for example). We hypothesized that mice that survived challenges with CIN-afflicted tumors
314 would show signs of an acquired immune response due to their high survival rate.
315
316 We collected convalescent serum from survivors to quantify *de novo* anti-cancer IgG antibodies
317 that may have resulted from successful rejection and clearance of CIN-afflicted tumors (**Fig. 4A**).
318 Sera was collected and then subsequently used in antibody binding testing and Western blotting
319 to confirm emergence of anti-B16F10 antibodies. We first quantified IgG2a and IgG2b titers in
320 convalescent sera, both of which have been previously found to engage mouse macrophage
321 Fcγ receptors (Bruhns, 2012; Nimmerjahn et al., 2010) that are typically required for
322 macrophage-mediated phagocytosis. B16F10 cells, either Tyrp1-expresing or Tyrp1 KO, were
323 incubated with sera (convalescent from survivors or naïve from unchallenged mice) and then
324 counterstained with conjugated antibodies against IgG2a/c and IgG2b (**Fig. 4B-i & ii**). All mice
325 that survived challenges from CIN-afflicted tumors yielded sera that showed significantly large
326 increases in IgG2a/c binding against both Tyrp1-positive and Tyrp1 KO B16F10 cells. We
327 similarly saw a statistically significant increases in IgG2b binding against both Tyrp1-positive and
328 Tyrp1 KO B16F10 cells using the same sera, although the increases in binding were more
329 variable. Altogether, we see that surviving CIN-afflicted tumors generates IgG-rich sera, like
330 previous studies (Dooling et al., 2022; Hayes et al., 2022). The increases in binding observed
331 against Tyrp1 KO cells also suggest that IgG antibodies target a repertoire of antigens beyond
332 Tyrp1, which we further qualitatively confirmed via Western blotting (**Fig. 4B-iii**). Convalescent
333 sera were used to immunoblot against B16F10 lysates, revealing many bands at multiple
334 molecular weights and more bands than when immunoblotting with naïve sera, supporting our
335 hypothesis of antigen broadening beyond Tyrp1. Lastly, we also tested IgG2a and IgG2b titers
336 from additional *in vivo* experiments: survivors from both titrated CIN-afflicted tumors from **Fig.**
337 **S6** and adoptive marrow transfers in **Fig. 3E**. Similarly, convalescent sera from all these mice
338 show increases in IgG2a/c and IgG2b in both Tyrp1-expressing and Tyrp1 KO B16F10 cells
339 (**Fig. S7**). These results confirm that regardless of the method used to exploit CIN, induction of
340 anti-cancer IgG can be expected.
341

342 To test where these *de novo* serum antibodies functionally promote macrophage-mediated
343 phagocytosis, we performed conventional 2D phagocytosis assays in which cancer cell
344 suspensions were opsonized with sera (or anti-Tyrp1 or mouse IgG2a isotype as controls) (**Fig.**
345 **4C-i**). Under conditions of CD47 KO, we see that nearly all unpurified convalescent sera
346 increased phagocytosis relative to naïve serum and mIgG2a isotype control. Furthermore, this
347 increase in phagocytosis is identical to that provided by anti-Tyrp1 (both ~5-fold higher than
348 baseline). We also find that sera continue to promote phagocytosis even in B16F10 CD47/Tyrp1
349 double KO cells (~3-fold higher than baseline). Convalescent sera are still able to provide
350 increases in phagocytosis against double KO cells, whereas anti-Tyrp1 expectedly does not
351 drive phagocytosis due to lack of antigen. This again supports the hypothesis of acquired
352 immunity with *de novo* IgG antibodies that target B16F10 antigens beyond Tyrp1. Upon
353 confirming the functional effect of *de novo* IgG in the convalescent sera, we then wondered if
354 convalescent serum IgG would be able to suppress tumoroid growth, given that this model better
355 captures both the biophysical microenvironment and proliferative capacity of tumors (Dooling et
356 al., 2022). Indeed, we found that convalescent serum IgG added simultaneously with
357 macrophages to B16F10 CD47 KO tumoroids led to either tumoroid elimination or significantly
358 suppressed growth (**Fig. 4C-ii**), although the efficacy was less potent as anti-Tyrp1. This
359 suggests that perhaps the polyclonal *de novo* IgGs here still lack the specificity benefits that
360 accompany a monoclonal antibody such as anti-Tyrp1. Nonetheless, these results demonstrate
361 induction of a generally potent anti-cancer antibody response B16F10 in a CD47 KO context.
362
363 We then proceeded to test the function of convalescent serum *in vivo* by opsonizing B16F10
364 CD47 KO cells just prior to subcutaneous implantation in naïve mice. For comparison, we also
365 opsonized B16F10 CD47 KO cells with either anti-Tyrp1 (positive control) or mIgG2a control
366 (negative control). We found that both convalescent sera and anti-Tyrp1 suppressed tumor
367 growth by days 11 and 13 relative to mIgG2a control (**Fig. 4D-i**). Interestingly, we found that
368 convalescent sera showed a trend of suppressing growth more than anti-Tyrp1, although this
369 was not statistically significant. We continued to monitor all mice for long-term survival, and we
370 found that this pre-opsonization with both convalescent sera and anti-Tyrp1 eliminated tumors
371 in challenged mice with near identical cure rates (25% and 22%, respectively) (**Fig. 4D-ii**).

372 Altogether, we found that the convalescent sera from mice originally challenged with
373 chromosomally unstable tumors has potent anti-cancer effects *in vitro* and *in vivo*.
374
375 **Acquired immunity suppresses growth of chromosomally stable tumors and becomes**
376 **more effective with ongoing challenges of CIN-afflicted tumors**
377 The anti-cancer IgG antibody development in survivors led us to further hypothesize that we
378 should see improved median survival and/or survival rate if surviving mice were re-challenged.
379 We therefore challenged surviving mice with a second injection of either DMSO-treated or
380 B16F10 CD47 KO cells (**Fig. 4E**). If additional survivors resulted from this experiment, we also
381 intended to undergo a third challenge, akin to a prime-boost strategy for anti-cancer vaccination.
382 It should be highlighted that starting from this second challenge, no mice received anti-Tyrp1.
383 This was done to maximally challenge acquired immunity and to better simulate the possibility
384 of recurrence post-therapy. Age-matched naïve mice receiving their first challenge responded
385 similarly to the younger cohorts (**Fig. 3B**). Of the previously cured mice, only a single mouse (of
386 11 total) survived a challenge with DMSO-treated B16F10 cells (**Fig. 4F**). However, median
387 survival increased (21 days) compared to their naïve counterparts (14 days), supporting the
388 initial hypothesis of prolonged survival. Survivors that were re-challenged again with MPS1i-
389 treated cells, however, showed 100% survival, even in the absence of anti-Tyrp1 (**Fig. 4F**). Age-
390 matched naïve mice receiving their first challenge of MPS1i-treated cells responded relatively
391 similarly (a single survivor out of 6 total, 17% survival) to the younger cohort (28% survival). This
392 complete success rate against a second challenge of CIN-afflicted B16F10 CD47 KO further
393 supports an acquired immune response, at least against ongoing chromosomally unstable cells.
394
395 Mice that failed to reject re-challenge tumors comprised of DMSO-treated B16F10 CD47 KO in
396 **Fig. 4F** were euthanized and had their tumors harvested to measure their immune cell infiltrate
397 by flow cytometry (**Fig. S8**). Although these mice did not survive, we found that these previous
398 survivors showed roughly a 2-fold increase in the number of immune cells in their tumors (**Fig.**
399 **4G-i**), a 2-fold increase in the number of CD3+ CD8+ T cells (**Fig. 4G-ii**), and a near 3-fold
400 increase in the number of F4/80+ macrophages (**Fig. 4G-iii**) compared to their naïve
401 counterparts. We further found that of the F4/80+ macrophage infiltrate, previous survivors had
402 roughly four times as many MHCII-high macrophages (M1-like, anti-cancer). These immune

403 infiltrate analyses suggest that although the acquired immune response in these previous
404 survivors was still not potent enough to clear chromosomally stable and regularly proliferating
405 B16F10 CD47 KO tumors, it did enhance cell-mediated immunity.
406
407 Lastly, we performed a third tumor challenge on second challenge survivors with untreated
408 B16F10 CD47 KO cells (chromosomally stable and regular proliferating). Mice were left
409 untreated post-challenge (no anti-Tyrp1). ~56% of these mice completely resisted tumor growth.
410 Of the four mice that developed tumors, two had to be euthanized prematurely due to tumor
411 rupture but were indeed showing signs of growth suppression. The last two mice consisted of
412 two long-term partial responders: one whose tumor did not reach terminal burden until 82 days
413 post-challenge and another who experienced stable tumor regression with almost no regrowth.
414 Overall, the 56% survival rate in the third challenge, in the absence of anti-Tyrp1, and the partial
415 responses observed in mice that grew tumors suggest a durable immunological response that
416 results from facing and clearing ongoing chromosomally unstable tumors, at least in the context
417 of CD47 disruption.
418
419
420
421
422

423 **Discussion**

424 Macrophage-oriented immunotherapies against solid tumors have maximal efficacy when three
425 elements are combined: large numbers of macrophages for cooperativity, IgG opsonization that
426 activates Fc receptors and stimulates macrophage-mediated phagocytosis, and disruption of the
427 CD47 macrophage immune checkpoint (Dooling et al., 2022). However, even with these factors
428 properly applied, complete tumor rejection and clearance is not guaranteed and varies greatly
429 across *in vivo* mouse studies (Andrechak et al., 2022; Dooling et al., 2022; Hayes et al., 2022;
430 Kamer et al., 2021). Here, we show a 97% survival rate of mice challenged with CIN-afflicted
431 B16F10 tumors when maximizing macrophage-mediated activity. This result improves upon
432 previous studies and is more impressive given that B16F10 are typically poorly immunogenic,
433 do not respond to either anti-CD47 or anti-PD-1/PD-L1 monotherapies, and show large variability
434 in cure rates (anywhere from 20-40%) even when macrophages should be maximally
435 phagocytic.
436
437 These results suggest that CIN in early stages generates anti-cancer vulnerabilities that favor
438 macrophage-mediated immune response, contingent on conditions of maximal phagocytosis.
439 Immunocompetent mice consistently survive these challenges at high survival rates. These
440 survivors also develop *de novo* anti-cancer IgG, similar to previous studies (Dooling et al., 2022;
441 Hayes et al., 2022), that are pro-phagocytic, multi-epitope, and efficacious *in vivo*. The
442 emergence of these IgGs could be synergistic with clinically relevant CD47 blockade treatments
443 for solid tumors and help address concerns regarding resistance due to antigen loss (Jalil et al.,
444 2020). Mice that are re-challenged with chromosomally stable CD47 KO tumors (and without
445 exogenous anti-Tyrp1 opsonization) shows increased median survival and increased immune
446 infiltrate, further supporting the hypothesis of newly generated anti-cancer acquired immunity.
447 More interestingly, though, we see that all mice re-challenged with CIN-afflicted CD47 KO
448 tumors survive, even in the absence of anti-Tyrp1 opsonization. A third challenge of these two-
449 time survivors with chromosomally stable CD47 KO tumors shows >50% mice survive and
450 improved median survival for non-survivors. These results elucidate two advantages that CIN
451 can provide to better therapeutic outcomes. First, early-stage CIN facilitates survival while
452 generating potent *de novo* IgGs that can drive positive phagocytic feedback to minimize
453 recurrence. Second, ongoing vulnerability-inducing CIN in tumor cells can both strengthen cell-

454 mediated acquired immunity and create an antigen reservoir for the maintenance of long-term
455 humoral immunity.
456
457 The effects of CIN and aneuploidy in macrophages nonetheless still require more investigation.
458 While secretome from MPS1i-treated cancer cells has been found to trigger expression of *Arg1*
459 and *Il6* (Xian et al., 2021), both of which are pro-cancer M2-like macrophage markers (Fernando
460 et al., 2014; Mujal et al., 2022), our findings suggest that polarization is much more complex.
461 Here, whole-tumor bulk RNA-sequencing hints at CIN-afflicted tumors having a macrophage
462 population that is both less anti-inflammatory and M2-like. Single-cell RNA-sequencing of
463 BMDMs treated with secretome from CIN-afflicted cells further suggests that CIN induces a
464 microenvironment that can pushes macrophages to a pro-inflammatory, anti-cancer phenotype
465 while minimizing polarization to a pro-cancer phenotype. Our transcriptomics analyses also align
466 more with deeper investigation that suggest additional markers are required for macrophage
467 polarization distinction (Jablonksi et al., 2015). We further confirm these findings by observing
468 increased surface protein expression of anti-cancer M1-like macrophages *in vitro* 3D tumoroid
469 co-cultures with CIN-afflicted cells and *in vivo* immune infiltrate experiments. Furthermore,
470 BMDMs show enhanced clearance of CIN-afflicted cells in 3D tumoroid phagocytosis assays.
471 Additionally, the aforementioned study (Xian et al., 2021) only found this trend in SKOV3 cells,
472 whereas their aneuploid fused B16 cells actually show decreased *Arg1* expression, suggesting
473 possible cell-intrinsic complications. Meta-analyses of aneuploid tumor genomics data from
474 TCGA also suggest reduced anti-cancer macrophage activity (Davoli et al., 2017; Xian et al.,
475 2021). Our study, however, distinctly highlights macrophage response at early timepoints of CIN,
476 during the which cancer cells have not yet adapted to CIN- and aneuploidy-induced stresses.
477 TCGA studies, on the other hand, are limited to much later timepoints when cells have overcome
478 to CIN- and aneuploidy-associated stresses and developed their own unique aneuploidies to
479 drive tumor progression. Additionally, more recent studies find that aneuploidy and CIN paired
480 with high tumor mutational burdens show increased median survival in patients (Spurr et al.,
481 2022a; Spurr et al., 2022b), suggesting possible other complexities that favor immune infiltration
482 and that could explain how CIN can favor macrophage-mediated immune response.
483
484

485 **References**

486 Ahn, J., Xia, T., Rabasa Capote, A., Betancourt, D., Barber, G.N., 2018. Extrinsic Phagocyte-
487 Dependent STING Signaling Dictates the Immunogenicity of Dying Cells. Cancer Cell 33,
488 862-873.e5. https://doi.org/10.1016/j.ccell.2018.03.027
489
490 Alvey, C.M., Spinler, K.R., Irianto, J., Pfeifer, C.R., Hayes, B., Xia, Y., Cho, S., Dingal, P.C.P.D.,
491 Hsu, J., Smith, L., Tewari, M., Discher, D.E., 2017. SIRPA-Inhibited, Marrow-Derived
492 Macrophages Engorge, Accumulate, and Differentiate in Antibody-Targeted Regression of
493 Solid Tumors. Current Biology 27, 2065-2077.e6. https://doi.org/10.1016/j.cub.2017.06.005
494
495 Andrechak, J.C., Dooling, L.J., Hayes, B.H., Kadu, S., Zhang, W., Pan, R., Vashisth, M., Irianto,
496 J., Alvey, C.M., Discher, D.E., 2022a. Cooperative phagocytosis underlies macrophage
497 immunotherapy of solid tumours and initiates a broad anti-tumour IgG response (preprint).
498 Bioengineering. https://doi.org/10.1101/2022.01.01.474150
499
500 Andrechak, J.C., Dooling, L.J., Tobin, M.P., Zhang, W., Hayes, B.H., Lee, J.Y., Jin, X., Irianto,
501 J., Discher, D.E., 2022b. CD47-SIRPα Checkpoint Disruption in Metastases Requires
502 Tumor-Targeting Antibody for Molecular and Engineered Macrophage Therapies. Cancers
503 14, 1930. https://doi.org/10.3390/cancers14081930
504
505 Ben-David, U., Amon, A., 2020. Context is everything: aneuploidy in cancer. Nat Rev Genet 21,
506 44–62. https://doi.org/10.1038/s41576-019-0171-x
507
508 Boilève, A., Senovilla, L., Vitale, I., Lissa, D., Martins, I., Métivier, D., van den Brink, S., Clevers,
509 H., Galluzzi, L., Castedo, M., Kroemer, G., 2013. Immunosurveillance against
510 tetraploidization-induced colon tumorigenesis. Cell Cycle 12, 473–479.
511 https://doi.org/10.4161/cc.23369
512
513 Bruhns, P., 2012. Properties of mouse and human IgG receptors and their contribution to
514 disease models. Blood 119, 5640–5649. https://doi.org/10.1182/blood-2012-01-380121
515
516 Cerezo-Wallis, D., Contreras-Alcalde, M., Troulé, K., Catena, X., Mucientes, C., Calvo, T.G.,
517 Cañón, E., Tejedo, C., Pennacchi, P.C., Hogan, S., Kölblinger, P., Tejero, H., Chen, A.X.,
518 Ibarz, N., Graña-Castro, O., Martinez, L., Muñoz, J., Ortiz-Romero, P., Rodriguez-Peralto,
519 J.L., Gómez-López, G., Al-Shahrour, F., Rabadán, R., Levesque, M.P., Olmeda, D.,
520 Soengas, M.S., 2020. Midkine rewires the melanoma microenvironment toward a
521 tolerogenic and immune-resistant state. Nat Med 26, 1865–1877.
522 https://doi.org/10.1038/s41591-020-1073-3
523

524 Champion, J.A., Mitragotri, S., 2006. Role of target geometry in phagocytosis. Proc. Natl. Acad.
525 Sci. U.S.A. 103, 4930–4934. https://doi.org/10.1073/pnas.0600997103
526
527 Chao, M.P., Jaiswal, S., Weissman-Tsukamoto, R., Alizadeh, A.A., Gentles, A.J., Volkmer, J.,
528 Weiskopf, K., Willingham, S.B., Raveh, T., Park, C.Y., Majeti, R., Weissman, I.L., 2010.
529 Calreticulin Is the Dominant Pro-Phagocytic Signal on Multiple Human Cancers and Is
530 Counterbalanced by CD47. Sci. Transl. Med. 2.
531 https://doi.org/10.1126/scitranslmed.3001375
532
533 Chunduri, N.K., Storchová, Z., 2019. The diverse consequences of aneuploidy. Nat Cell Biol 21,
534 54–62. https://doi.org/10.1038/s41556-018-0243-8
535
536 Cohen-Sharir, Y., McFarland, J.M., Abdusamad, M., Marquis, C., Bernhard, S.V., Kazachkova,
537 M., Tang, H., Ippolito, M.R., Laue, K., Zerbib, J., Malaby, H.L.H., Jones, A., Stautmeister,
538 L.-M., Bockaj, I., Wardenaar, R., Lyons, N., Nagaraja, A., Bass, A.J., Spierings, D.C.J.,
539 Foijer, F., Beroukhim, R., Santaguida, S., Golub, T.R., Stumpff, J., Storchová, Z., Ben-
540 David, U., 2021. Aneuploidy renders cancer cells vulnerable to mitotic checkpoint inhibition.
541 Nature 590, 486–491. https://doi.org/10.1038/s41586-020-03114-6
542
543 Crasta, K., Ganem, N.J., Dagher, R., Lantermann, A.B., Ivanova, E.V., Pan, Y., Nezi, L.,
544 Protopopov, A., Chowdhury, D., Pellman, D., 2012. DNA breaks and chromosome
545 pulverization from errors in mitosis. Nature 482, 53–58. https://doi.org/10.1038/nature10802
546
547 Cunha, L.D., Yang, M., Carter, R., Guy, C., Harris, L., Crawford, J.C., Quarato, G., Boada-
548 Romero, E., Kalkavan, H., Johnson, M.D.L., Natarajan, S., Turnis, M.E., Finkelstein, D.,
549 Opferman, J.T., Gawad, C., Green, D.R., 2018. LC3-Associated Phagocytosis in Myeloid
550 Cells Promotes Tumor Immune Tolerance. Cell 175, 429-441.e16.
551 https://doi.org/10.1016/j.cell.2018.08.061
552
553 Davoli, T., Uno, H., Wooten, E.C., Elledge, S.J., 2017. Tumor aneuploidy correlates with markers
554 of immune evasion and with reduced response to immunotherapy. Science 355, eaaf8399.
555 https://doi.org/10.1126/science.aaf8399
556
557 Fernando, M.R., Reyes, J.L., Iannuzzi, J., Leung, G., McKay, D.M., 2014. The Pro-Inflammatory
558 Cytokine, Interleukin-6, Enhances the Polarization of Alternatively Activated Macrophages.
559 PLoS ONE 9, e94188. https://doi.org/10.1371/journal.pone.0094188
560
561 Georgouli, M., Herraiz, C., Crosas-Molist, E., Fanshawe, B., Maiques, O., Perdrix, A., Pandya,
562 P., Rodriguez-Hernandez, I., Ilieva, K.M., Cantelli, G., Karagiannis, P., Mele, S., Lam, H.,
563 Josephs, D.H., Matias-Guiu, X., Marti, R.M., Nestle, F.O., Orgaz, J.L., Malanchi, I.,

564 Fruhwirth, G.O., Karagiannis, S.N., Sanz-Moreno, V., 2019. Regional Activation of Myosin
565 II in Cancer Cells Drives Tumor Progression via a Secretory Cross-Talk with the Immune
566 Microenvironment. Cell 176, 757-774.e23. https://doi.org/10.1016/j.cell.2018.12.038
567 Harding, S.M., Benci, J.L., Irianto, J., Discher, D.E., Minn, A.J., Greenberg, R.A., 2017. Mitotic
568 progression following DNA damage enables pattern recognition within micronuclei. Nature
569 548, 466–470. https://doi.org/10.1038/nature23470
570
571 Hayes, B.H., Tsai, R.K., Dooling, L.J., Kadu, S., Lee, J.Y., Pantano, D., Rodriguez, P.L.,
572 Subramanian, S., Shin, J.-W., Discher, D.E., 2020. Macrophages show higher levels of
573 engulfment after disruption of *cis* interactions between CD47 and the checkpoint receptor
574 SIRPα. Journal of Cell Science 133, jcs237800. https://doi.org/10.1242/jcs.237800
575
576 Hayes, B.H., Zhu, H., Andrechak, J.C., Discher, D.E., 2022. Titrating CD47 by mismatch
577 CRISPRi reveals incomplete repression can eliminate IgG-opsonized tumors but CD47
578 heterogeneity limits induction of anti-tumor IgG (preprint). Cancer Biology.
579 https://doi.org/10.1101/2022.09.27.509740
580
581 Ingram, J.R., Blomberg, O.S., Sockolosky, J.T., Ali, L., Schmidt, F.I., Pishesha, N., Espinosa,
582 C., Dougan, S.K., Garcia, K.C., Ploegh, H.L., Dougan, M., 2017. Localized CD47 blockade
583 enhances immunotherapy for murine melanoma. Proc. Natl. Acad. Sci. U.S.A. 114, 10184–
584 10189. https://doi.org/10.1073/pnas.1710776114
585
586 Jablonski, K.A., Amici, S.A., Webb, L.M., Ruiz-Rosado, J. de D., Popovich, P.G., Partida-
587 Sanchez, S., Guerau-de-Arellano, M., 2015. Novel Markers to Delineate Murine M1 and M2
588 Macrophages. PLoS ONE 10, e0145342. https://doi.org/10.1371/journal.pone.0145342
589
590 Jalil, A.R., Andrechak, J.C., Discher, D.E., 2020. Macrophage checkpoint blockade: results from
591 initial clinical trials, binding analyses, and CD47-SIRPα structure–function. Antibody
592 Therapeutics 3, 80–94. https://doi.org/10.1093/abt/tbaa006
593
594 Kamber, R.A., Nishiga, Y., Morton, B., Banuelos, A.M., Barkal, A.A., Vences-Catalán, F., Gu,
595 M., Fernandez, D., Seoane, J.A., Yao, D., Liu, K., Lin, S., Spees, K., Curtis, C., Jerby-Arnon,
596 L., Weissman, I.L., Sage, J., Bassik, M.C., 2021. Inter-cellular CRISPR screens reveal
597 regulators of cancer cell phagocytosis. Nature 597, 549–554.
598 https://doi.org/10.1038/s41586-021-03879-4
599
600 Kitajima, S., Tani, T., Springer, B.F., Campisi, M., Osaki, T., Haratani, K., Chen, M., Knelson,
601 E.H., Mahadevan, N.R., Ritter, J., Yoshida, R., Köhler, J., Ogino, A., Nozawa, R.-S.,
602 Sundararaman, S.K., Thai, T.C., Homme, M., Piel, B., Kivlehan, S., Obua, B.N., Purcell, C.,
603 Yajima, M., Barbie, T.U., Lizotte, P.H., Jänne, P.A., Paweletz, C.P., Gokhale, P.C., Barbie,

604 D.A., 2022. MPS1 inhibition primes immunogenicity of KRAS-LKB1 mutant lung cancer.
605 Cancer Cell 40, 1128-1144.e8. https://doi.org/10.1016/j.ccell.2022.08.015
606
607 Klichinsky, M., Ruella, M., Shestova, O., Lu, X.M., Best, A., Zeeman, M., Schmierer, M.,
608 Gabrusiewicz, K., Anderson, N.R., Petty, N.E., Cummins, K.D., Shen, F., Shan, X., Veliz,
609 K., Blouch, K., Yashiro-Ohtani, Y., Kenderian, S.S., Kim, M.Y., O'Connor, R.S., Wallace,
610 S.R., Kozlowski, M.S., Marchione, D.M., Shestov, M., Garcia, B.A., June, C.H., Gill, S.,
611 2020. Human chimeric antigen receptor macrophages for cancer immunotherapy. Nat
612 Biotechnol 38, 947–953. https://doi.org/10.1038/s41587-020-0462-y
613
614 Krysko, D.V., Ravichandran, K.S., Vandenabeele, P., 2018. Macrophages regulate the
615 clearance of living cells by calreticulin. Nat Commun 9, 4644.
616 https://doi.org/10.1038/s41467-018-06807-9
617
618 Mackenzie, K.J., Carroll, P., Martin, C.-A., Murina, O., Fluteau, A., Simpson, D.J., Olova, N.,
619 Sutcliffe, H., Rainger, J.K., Leitch, A., Osborn, R.T., Wheeler, A.P., Nowotny, M., Gilbert, N.,
620 Chandra, T., Reijns, M.A.M., Jackson, A.P., 2017. cGAS surveillance of micronuclei links
621 genome instability to innate immunity. Nature 548, 461–465.
622 https://doi.org/10.1038/nature23449
623
624 Mallin, M.M., Kim, N., Choudhury, M.I., Lee, S.J., An, S.S., Sun, S.X., Konstantopoulos, K.,
625 Pienta, K.J., Amend, S.R., 2022. Cells in the Polyaneuploid Cancer Cell (PACC) state have
626 increased metastatic potential (preprint). Cancer Biology.
627 https://doi.org/10.1101/2022.09.16.508155
628
629 Morrissey, M.A., Kern, N., Vale, R.D., 2020. CD47 Ligation Repositions the Inhibitory Receptor
630 SIRPA to Suppress Integrin Activation and Phagocytosis. Immunity 53, 290-302.e6.
631 https://doi.org/10.1016/j.immuni.2020.07.008
632
633 Mujal, A.M., Combes, A.J., Rao, A.A., Binnewies, M., Samad, B., Tsui, J., Boissonnas, A.,
634 Pollack, J.L., Argüello, R.J., Meng, M.V., Porten, S.P., Ruhland, M.K., Barry, K.C., Chan, V.,
635 Krummel, M.F., 2022. Holistic Characterization of Tumor Monocyte-to-Macrophage
636 Differentiation Integrates Distinct Immune Phenotypes in Kidney Cancer. Cancer
637 Immunology Research 10, 403–419. https://doi.org/10.1158/2326-6066.CIR-21-0588
638
639 Nia, H.T., Munn, L.L., Jain, R.K., 2020. Physical traits of cancer. Science 370, eaaz0868.
640 https://doi.org/10.1126/science.aaz0868
641

642 Nimmerjahn, F., Lux, A., Albert, H., Woigk, M., Lehmann, C., Dudziak, D., Smith, P., Ravetch,
643 J.V., 2010. FcγRIV deletion reveals its central role for IgG2a and IgG2b activity in vivo. Proc.
644 Natl. Acad. Sci. U.S.A. 107, 19396–19401. https://doi.org/10.1073/pnas.1014515107
645
646 Noy, R., Pollard, J.W., 2014. Tumor-Associated Macrophages: From Mechanisms to Therapy.
647 Immunity 41, 49–61. https://doi.org/10.1016/j.immuni.2014.06.010
648
649 Oldenborg, P.-A., Zheleznyak, A., Fang, Y.-F., Lagenaur, C.F., Gresham, H.D., Lindberg, F.P.,
650 2000. Role of CD47 as a Marker of Self on Red Blood Cells. Science 288, 2051–2054.
651 https://doi.org/10.1126/science.288.5473.2051
652
653 Perry, J.S.A., Morioka, S., Medina, C.B., Iker Etchegaray, J., Barron, B., Raymond, M.H., Lucas,
654 C.D., Onengut-Gumuscu, S., Delpire, E., Ravichandran, K.S., 2019. Interpreting an
655 apoptotic corpse as anti-inflammatory involves a chloride sensing pathway. Nat Cell Biol 21,
656 1532–1543. https://doi.org/10.1038/s41556-019-0431-1
657
658 Santaguida, S., Richardson, A., Iyer, D.R., M'Saad, O., Zasadil, L., Knouse, K.A., Wong, Y.L.,
659 Rhind, N., Desai, A., Amon, A., 2017. Chromosome Mis-segregation Generates Cell-Cycle-
660 Arrested Cells with Complex Karyotypes that Are Eliminated by the Immune System.
661 Developmental Cell 41, 638-651.e5. https://doi.org/10.1016/j.devcel.2017.05.022
662
663 Senovilla, L., Vitale, I., Martins, I., Tailler, M., Pailleret, C., Michaud, M., Galluzzi, L., Adjemian,
664 S., Kepp, O., Niso-Santano, M., Shen, S., Mariño, G., Criollo, A., Boilève, A., Job, B.,
665 Ladoire, S., Ghiringhelli, F., Sistigu, A., Yamazaki, T., Rello-Varona, S., Locher, C., Poirier-
666 Colame, V., Talbot, M., Valent, A., Berardinelli, F., Antoccia, A., Ciccosanti, F., Fimia, G.M.,
667 Piacentini, M., Fueyo, A., Messina, N.L., Li, M., Chan, C.J., Sigl, V., Pourcher, G.,
668 Ruckenstuhl, C., Carmona-Gutierrez, D., Lazar, V., Penninger, J.M., Madeo, F., López-Otín,
669 C., Smyth, M.J., Zitvogel, L., Castedo, M., Kroemer, G., 2012. An Immunosurveillance
670 Mechanism Controls Cancer Cell Ploidy. Science 337, 1678–1684.
671 https://doi.org/10.1126/science.1224922
672
673 Sockolosky, J.T., Dougan, M., Ingram, J.R., Ho, C.C.M., Kauke, M.J., Almo, S.C., Ploegh, H.L.,
674 Garcia, K.C., 2016. Durable antitumor responses to CD47 blockade require adaptive
675 immune stimulation. Proc. Natl. Acad. Sci. U.S.A. 113.
676 https://doi.org/10.1073/pnas.1604268113
677
678 Spurr, L.F., Martinez, C.A., Kang, W., Chen, M., Zha, Y., Hseu, R., Gutiontov, S.I., Turchan,
679 W.T., Lynch, C.M., Pointer, K.B., Chang, P., Murgu, S., Husain, A.N., Cody, B., Vokes, E.E.,
680 Bestvina, C.M., Patel, J.D., Diehn, M., Gajewski, T.F., Weichselbaum, R.R., Chmura, S.J.,
681 Pitroda, S.P., 2022a. Highly aneuploid non-small cell lung cancer shows enhanced

682 responsiveness to concurrent radiation and immune checkpoint blockade. Nat Cancer 3,
683 1498–1512. https://doi.org/10.1038/s43018-022-00467-x
684
685 Spurr, L.F., Weichselbaum, R.R., Pitroda, S.P., 2022b. Tumor aneuploidy predicts survival
686 following immunotherapy across multiple cancers. Nat Genet 54, 1782–1785.
687 https://doi.org/10.1038/s41588-022-01235-4
688
689 Suter, E.C., Schmid, E.M., Harris, A.R., Voets, E., Francica, B., Fletcher, D.A., 2021.
690 Antibody:CD47 ratio regulates macrophage phagocytosis through competitive receptor
691 phosphorylation. Cell Reports 36, 109587. https://doi.org/10.1016/j.celrep.2021.109587
692
693 Taylor, A.M., Shih, J., Ha, G., Gao, G.F., Zhang, X., Berger, A.C., Schumacher, S.E., Wang, C.,
694 Hu, H., Liu, Jianfang, The Cancer Genome Atlas Reseach Network, Lazar, A.J., Cherniack,
695 A.D., Beroukhim, R., Meyerson, M., 2018. Genomic and Functional Approaches to
696 Understanding Cancer Aneuploidy. Cancer Cell 33, 676-689.e3.
697 https://doi.org/10.1016/j.ccell.2018.03.007
698
699 Tripathi, R., Modur, V., Senovilla, L., Kroemer, G., Komurov, K., 2019. Suppression of tumor
700 antigen presentation during aneuploid tumor evolution contributes to immune evasion.
701 OncoImmunology 8, 1657374. https://doi.org/10.1080/2162402X.2019.1657374
702
703 Tsai, R.K., Discher, D.E., 2008. Inhibition of “self” engulfment through deactivation of myosin-II
704 at the phagocytic synapse between human cells. Journal of Cell Biology 180, 989–1003.
705 https://doi.org/10.1083/jcb.200708043
706
707 Vasudevan, A., Baruah, P.S., Smith, J.C., Wang, Z., Sayles, N.M., Andrews, P., Kendall, J., Leu,
708 J., Chunduri, N.K., Levy, D., Wigler, M., Storchová, Z., Sheltzer, J.M., 2020. Single-
709 Chromosomal Gains Can Function as Metastasis Suppressors and Promoters in Colon
710 Cancer. Developmental Cell 52, 413-428.e6. https://doi.org/10.1016/j.devcel.2020.01.034
711
712 Vasudevan, A., Schukken, K.M., Sausville, E.L., Girish, V., Adebambo, O.A., Sheltzer, J.M.,
713 2021. Aneuploidy as a promoter and suppressor of malignant growth. Nat Rev Cancer 21,
714 89–103. https://doi.org/10.1038/s41568-020-00321-1
715
716 Wang, R.W., Viganò, S., Ben-David, U., Amon, A., Santaguida, S., 2021. Aneuploid senescent
717 cells activate NF-κB to promote their immune clearance by NK cells. EMBO Reports 22.
718 https://doi.org/10.15252/embr.202052032
719
720 Willingham, S.B., Volkmer, J.-P., Gentles, A.J., Sahoo, D., Dalerba, P., Mitra, S.S., Wang, J.,
721 Contreras-Trujillo, H., Martin, R., Cohen, J.D., Lovelace, P., Scheeren, F.A., Chao, M.P.,

722 Weiskopf, K., Tang, C., Volkmer, A.K., Naik, T.J., Storm, T.A., Mosley, A.R., Edris, B.,
723 Schmid, S.M., Sun, C.K., Chua, M.-S., Murillo, O., Rajendran, P., Cha, A.C., Chin, R.K.,
724 Kim, D., Adorno, M., Raveh, T., Tseng, D., Jaiswal, S., Enger, P.Ø., Steinberg, G.K., Li, G.,
725 So, S.K., Majeti, R., Harsh, G.R., van de Rijn, M., Teng, N.N.H., Sunwoo, J.B., Alizadeh,
726 A.A., Clarke, M.F., Weissman, I.L., 2012. The CD47-signal regulatory protein alpha (SIRPa)
727 interaction is a therapeutic target for human solid tumors. Proc. Natl. Acad. Sci. U.S.A. 109,
728 6662–6667. https://doi.org/10.1073/pnas.1121623109
729
730 Xian, S., Dosset, M., Almanza, G., Searles, S., Sahani, P., Waller, T.C., Jepsen, K., Carter, H.,
731 Zanetti, M., 2021. The unfolded protein response links tumor aneuploidy to local immune
732 dysregulation. EMBO Rep 22. https://doi.org/10.15252/embr.202152509
733
734 Zhou, Y., Fei, M., Zhang, G., Liang, W.-C., Lin, W., Wu, Y., Piskol, R., Ridgway, J., McNamara,
735 E., Huang, H., Zhang, J., Oh, J., Patel, J.M., Jakubiak, D., Lau, J., Blackwood, B., Bravo,
736 D.D., Shi, Y., Wang, J., Hu, H.-M., Lee, W.P., Jesudason, R., Sangaraju, D., Modrusan, Z.,
737 Anderson, K.R., Warming, S., Roose-Girma, M., Yan, M., 2020. Blockade of the Phagocytic
738 Receptor MerTK on Tumor-Associated Macrophages Enhances P2X7R-Dependent STING
739 Activation by Tumor-Derived cGAMP. Immunity 52, 357-373.e9.
740 https://doi.org/10.1016/j.immuni.2020.01.014
741
742

743 **Materials and Methods**

744

745 **Cell culture**

746 B16F10 cells (CRL-6475) were obtained from American Type Culture Collection (ATCC) and
747 cultured at 37°C and 5% CO_2 in either RPMI-1640 (Gibco 11835-030) or Dulbecco's Modified
748 Eagle Medium (DMEM, Gibco 10569-010) supplemented with 10% fetal bovine serum (FBS,
749 Sigma F2442), 100 U/ mL penicillin and 100 µg/mL streptomycin (1% P/S, Gibco 15140-122).
750 B16F10 cells were maintained in passage in RPMI-1640 but switched to DMEM at least three
751 days prior to *in vivo* subcutaneous injections. 293T human embryonic kidney (CRL-1573) cells
752 were also obtained from ATCC and cultured at 37°C and 5% CO_2 in DMEM culture media
753 supplemented with 10% FBS and 1% P/S. All cell lines were passaged every 2-3 days when a
754 confluency of ~80% was reached. For trypsinization, cells were washed once with Dulbecco's
755 phosphate-buffered saline (PBS, Gibco 14190-136) and then detached with 0.05% Trypsin
756 (Gibco 25300-054) for 5 min at 37°C and 5% CO_2. Trypsin was quenched with an equal volume
757 of complete culture media.

758

759 **Lentiviral production and transduction**

760 24 h prior to lentivirus production, 293T cells were plated at a density of $8x10^5$ cells in 2 mL of
761 DMEM in individual wells of a 6-well plate. On the day of transfection, 1.35 µg of psPAX2, 165
762 ng of pCMV-VSV-G, and 1.5 µg of lentiviral plasmid were added into a microcentrifuge tube with
763 7.5 µL of Mirus TransIT-Lenti transfection reagent (Mirus Bio, 6604). Once all plasmids were
764 pooled together with the transfection reagent, 300 µL of serum-free media was added. The
765 solution was gently mixed by pipetting and then allowed to incubate for 30 min. After 30 min
766 elapsed, the solution was gently added dropwise by pipetting to an individual 6-well containing
767 the 293T cells plated the day prior. We note that we also use B16F10 CD47 and Tyrp1 KO lines
768 in this study, whose preparation has been previously described (Hayes, et al., 2020). LentiV-
769 cas9_puro and Lenti_sgRNA_EFS_GFP plasmids (Addgene #108100 and 65656, respectively)
770 were gifts from Christopher Vakoc. psPAX2 was a gift from Didier Trono (Addgene plasmid
771 #12260). pVSV-G was a gift from Bob Weinberg (Addgene plasmid #8454). The single guide
772 RNA (sgRNA) oligonucleotides (CD47, 5′-TCCCCGTAGAGATTACAATG-3′; SIRPα, 5′-

773 TAATTCTAAGGTCATCTGCG-3′) were designed using the Broad CRISPR algorithm. sgRNAs
774 were cloned into the sgRNA vector using a BsmBI restriction digest.
775
776 Viral production was allowed to continue for 48 h, after which the supernatant was collected from
777 each well and centrifuged for 5 min at 300 x *g*. The supernatant was collected and then either
778 added directly to B16F10 cells (0.5 mL of lentivirus-containing supernatant to $2x10^4$ cells in an
779 individual 6-well) or stored at -70°C for long-term storage. 72 h after transduction, spent media
780 with lentivirus was aspirated, B16F10 cells were washed with PBS, and fresh media was added.
781 For selecting successfully lentivirally transduced cells, cells were cultured in fresh media
782 containing 1 µg/mL of puromycin (Invitrogen A1113803). Cells were kept in puromycin-
783 containing until a non-transduced control population also treated with puromycin completely
784 died.
785
786 **Antibodies**
787 Antibodies used for *in vivo* treatment and blocking and for *in vitro* phagocytosis are as follows:
788 anti-mouse/human Tyrp1 clone TA99 (BioXCell BE0151), mouse IgG2a isotype control clone
789 C1.18.4 (BioXCell BE0085), and Ultra-LEAF anti-mouse CD172a (SIRPα) clone P84
790 (BioLegend 144036). Low-endotoxin and preservative-free antibody preparations were used for
791 *in vivo* treatments and *in vitro* phagocytosis experiments. For primary antibody staining of
792 surface proteins via flow cytometry, the following were used: anti-mouse CD47 clone MIAP301
793 (BioXCell BE0270) and anti-mouse/human Tyrp1 clone TA99. Secondary antibodies used for
794 flow cytometry are as follows: Alexa Fluor 647 donkey anti-mouse IgG (ThermoFisher A-31571)
795 and Alexa Fluor 647 goat anti-rat IgG (ThermoFisher A-21247). All secondary antibody
796 concentrations used followed the manufacturer's recommendations.
797
798 For immune infiltrate analysis, the following BioLegend antibodies were used: Brilliant Violet 650
799 anti-mouse CD45 clone 30-F11 (103151), Brilliant Violet 785 anti-mouse CD45 clone 30-F11
800 (103149), APC/Cy7 anti-mouse CD45 clone 30-F11 (103115), APC anti-mouse/human CD11b
801 clone M1/70 (101212), PE/Cyanine7 anti-mouse/human CD11b clone M1/70 (101216),
802 PE/Dazzle 594 anti-mouse Ly6G clone 1A8 (127647), PerCP anti-mouse Ly-6G clone 1A8
803 (127653), PE anti-mouse F4/80 clone BM8 (123110), Brilliant Violet 605 anti-mouse Ly-6C clone

804 HK1.4 (128035), APC anti-mouse I-A/I-E clone M5/114.15.2 (107614), Pacific Blue anti-mouse
805 CD86 clone GL-1 (105022), APC/Cy7 anti-mouse CD86 clone GL-1 (105029), APC anti-mouse
806 CD206 (MMR) clone C068C2 (141707), Brilliant Violet 421 anti-mouse CD206 clone C068C2
807 (141717), PE/Cy7 anti-mouse CD163 clone S15049F (156707), APC/Cy7 anti-mouse CD3e
808 clone 145-2C11 (100329), and Alexa Fluor 647 anti-mouse CD8a clone 53-6.7 (100727).
809 TruStain FcX PLUS (anti-mouse CD16/32) clone S17011E (156603) was used in all immune
810 infiltrate experiments to block Fc receptors. For immunogenicity post-MPS1i treatment, APC
811 anti-mouse H-2kb/H-2Db clone 28-8-6 (114613) was used. For IgG titer in tumor challenge
812 surviving mice, the following BioLegend antibodies were used: PE anti-mouse IgG2a clone
813 RMG2a-62 (407108, known to bind IgG2c as well) and APC anti-mouse IgG2b clone RMG2b-1
814 (406711). Primary antibody used in Western blotting was anti-β-actin clone C4 (Santa Cruz sc
815 47778). Secondary antibody used in Western blotting was HRP sheep anti-mouse IgG (GE Life
816 Sciences NA931V).
817
818 **Mice**
819 C57BL/6 mice (Jackson Laboratory 000664) were 6-12 weeks old at the time of tumor challenges
820 and for bone marrow harvesting, with the exception of second and third challenge experiments.
821 Additionally, for re-challenge experiments, age-matched naïve mice were used. All experiments
822 were performed in accordance with protocols approved by the Institutional Animal Care and Use
823 Committee (IACUC) of the University of Pennsylvania.
824
825 **Drug treatments & micronuclei quantification**
826 For MPS1i studies, the following chemical drugs were used: reversine (Cayman Chemical
827 10004412), AZ3146 (Cayman Chemical 19991), and BAY 12-17389 (Selleck Chemicals S8215).
828 24 h prior to treatment, B16F10 cells were in either 6-well or 12-well plates. For 6-wells, 20,000
829 cells were plated per well. For 12-wells, 2,000 cells were plated per well. On the day of treatment,
830 spent media was aspirated, and fresh media supplemented with 10% FBS, 1% P/S, and either
831 MPS1i or DMSO vehicle control was added to each well. The concentration used for each
832 treatment is listed in the Figure legend. The volume of DMSO added was equal to the volume
833 required for the highest MPS1i concentration for each experiment. All cells were treated for 24
834 h, after which drug-containing spent media was aspirated. Cells were then washed with a full

835 volume of PBS for 5 min. PBS was aspirated, and two repeat washes were performed. Cells
836 were then allowed to recover from MPS1i treatment for an additional 48 h, with a fresh media
837 replacement 24 h after the initial wash.
838
839 For imaging and micronuclei quantification, cells were fixed with 4% formaldehyde for 20 min
840 after the 48 h recovery period and later imaged on an Olympus IX inverted microscope with a
841 40x/0.6 NA objective. The Olympus IX microscope was equipped with a Prime sCMOS camera
842 (Photometrics) and a pE-300 LED illuminator (CoolLED) and was controlled with MicroManager
843 software v2. At least 200 B16F10 were imaged per individual well for micronuclei quantification.
844
845 **Bone marrow-derived macrophages (BMDMs)**
846 Bone marrow was harvested from the femurs and tibia of donor mice, lysed with ACK buffer
847 (Gibco A1049201) to deplete red blood cells, and then cultured on Petri culture dishes for 7 days
848 in Iscove's Modified Dulbecco's Medium (IMDM, Gibco 12440-053) supplemented with 10%
849 FBS, 1% P/S, and 20 ng/mL recombinant mouse macrophage colony-stimulating factor (M-CSF,
850 BioLegend 576406). 72 h after initial plating, one whole volume of fresh IMDM supplemented
851 10% FBS, 1% P/S, and 20 ng/mL M-CSF. After 7 days of differentiation, spent media was
852 removed, BMDMs were gently washed once with phosphate-buffered saline (PBS), and fresh
853 IMDM supplemented with 10% FBS, 1% P/S, and 20 ng/mL M-CSF was added.
854
855 **Conditioned media treatment of BMDMs**
856 BMDMs that had successfully undergone 7 days of differentiation in 20 ng/mL M-CSF were used.
857 Spent media was removed, BMDMs were gently washed once with phosphate-buffered saline
858 (PBS), and fresh IMDM supplemented 10% FBS, 1% P/S, and 20 ng/mL M-CSF was added.
859 Then, conditioned media from B16F10 cells treated with either MPS1i or DMSO was collected.
860 Conditioned media was centrifuged for 5 min at 300 x *g* to remove any cellular debris. The
861 supernatant was collected and then supplemented to 5% FBS, 1% P/S, and 20 ng/mL M-CSF.
862 One whole volume of conditioned media was added to BMDMs with fresh media. 24 h after
863 treatment, BMDMs were detached using 0.05% Trypsin and processed for single-cell RNA-
864 sequencing.
865

866 ***In vitro* phagocytosis**

867 For two-dimensional phagocytosis assays, BMDMs were detached using 0.05% Trypsin and re-
868 plated in either 6-well or 12-well plates, at a density of $1.8x10^4$ cells per cm^2 in IMDM
869 supplemented 10% FBS, 1% P/S, and 20 ng/mL M-CSF. After 24 h elapsed, BMDMs were
870 labeled with 0.5 μM CellTracker DeepRed dye (Invitrogen C34565), according to the
871 manufacturer's protocol. Following staining, BMDMs were washed and incubated in serum-free
872 IMDM supplemented 0.1% (w/v) BSA and 1% P/S. B16F10 cells were labeled with
873 carboxyfluorescein diacetate succinimidyl ester (Vybrant CFDA-SE Cell Tracer, Invitrogen
874 V12883), also according to the manufacturer's protocol. B16F10 cells were detached and
875 opsonized with 10 μg/mL anti-Tyrp1, with 10 μg/mL mouse IgG2a isotype control antibody, or
876 5% (v/v) mouse serum in 1% BSA. Opsonization was allowed for 30-45 min on ice. Opsonized
877 B16F10 suspensions were then added to BMDMs at a ~2:1 ratio and incubated at 37°C and 5%
878 CO_2 for 2 h. Non-adherent cells were removed by gently washing with PBS. For imaging, cells
879 were fixed with 4% formaldehyde for 20 min and later imaged on an Olympus IX inverted
880 microscope with a 40x/0.6 NA objective. The Olympus IX microscope was equipped with a Prime
881 sCMOS camera (Photometrics) and a pE-300 LED illuminator (CoolLED) and was controlled
882 with MicroManager software v2. At least 300 macrophages were imaged per individual well for
883 calculation of phagocytosis.

884

885 **3D tumoroid formation and phagocytosis**

886 Briefly, non-TC-treated 96-well U-bottom plates were treated with 100 μL of anti-adherence
887 rinsing solution (StemCell Technologies 07010) for 1 h. The cells were then washed with 100 μL
888 of complete RPMI 1640 cell culture media. This generated surfaces conducive to generating
889 tumoroids and preventing cells from adhering to the well bottom during experiments. B16F10
890 were detached by brief trypsinization, resuspended at a concentration of $1x10^4$ cells per mL in
891 complete RPMI 1640 cell culture media (10% FBS, 1% P/S) with 50 μM β-mercaptoethanol
892 (Gibco 21985023). 100 μL of this cell suspension was added to each well such that each
893 tumoroid initially started with approximately $1x10^3$ cells. Aggregation of B16F10 cells was
894 confirmed 24 h later by inspection under microcopy. Upon confirmation of tumoroid formation,
895 BMDMs were labeled with 0.5 μM CellTracker DeepRed dye (Invitrogen C34565), according to
896 the manufacturer's protocol. BMDMs were then detached by brief trypsinization and gentle

897 scraping and resuspended in complete RPMI 1640 cell culture media at a concentration that
898 would allow for delivery of $3x10^3$ BMDMs to each individual tumoroid culture. The BMDM cell
899 suspension was also supplemented with 120 ng/mL M-CSF and antibodies (either anti-Tyrp1 or
900 mouse IgG2a isotype control) such that delivery of 20 µL of this suspension to each individual
901 tumoroid culture result in final concentrations of 20 ng/mL M-CSF and 20 µg/mL of antibody. For
902 tumoroid studies in which mouse convalescent serum was used, the BMDM cell suspension was
903 supplemented with 120 ng/mL M-CSF and serum such that delivery of 20 µL of this suspension
904 to each individual tumoroid culture resulted in final concentrations of 20 ng/mL M-CSF and a
905 final mouse serum concentration of 1:200. Tumoroids were imaged on an Olympus IX inverted
906 microscope with a 4x/0.6 NA objective.
907
908 For macrophage polarization tumoroid experiments (Fig. 2B-C), B16F10 tumoroids were
909 prepared in the same manner as described above, with the exception that no anti-Tyrp1 or
910 mIgG2a was added. After 5 days had elapsed for the experiment, tumoroids were dissociated
911 by brief trypsinization and stained with conjugated antibodies targeting MHCII, CD86, CD163,
912 and CD206, following the manufacturer's protocol. Cells were then run on a BD LSRII (Benton
913 Dickinson) flow cytometer. Data were analyzed with FCS Express 7 software (De Novo
914 Software).
915
916 ***In vivo* tumor models**
917 B16F10 cells cultured in DMEM growth media were detached by brief trypsinization, washed
918 twice with PBS, and resuspended at $2x10^6$ cells per mL. Cell suspensions were kept on ice until
919 injection. All subcutaneous injections were performed on the right flank while mice were
920 anesthetized under isoflurane. Fur on the injection site was wet slightly with a drop of 70%
921 ethanol and brushed aside to better visualize the skin. A 100 µL bolus containing $2x10^5$ cells
922 cancer cells was injected beneath the skin. For treatments, mice received either intravenous or
923 intraperitoneal injections of anti-Tyrp1 clone TA99 or mouse IgG2a isotype control clone C1.18.4
924 (250 µg antibody in 100 µL PBS) on days 4, 5, 7, 9, 11, 13, and 15 post-tumor challenge.
925 Intravenous injections were done via the lateral tail vein. Tumors were monitored by palpation
926 and measured with digital calipers. The projected area was roughly elliptical and was calculated
927 as $A = \pi/4 \times L \times W$, where L is the length along the longest axis and W is the width measured

928 along the perpendicular axis. For our studies, a projected area of 125 mm^2 was considered
929 terminal burden for survival analyses. Mice were humanely euthanized following IACUC
930 protocols if tumor size reached 2.0 cm on either axis, if tumor reached a projected area greater
931 than 200 mm^2 or if a tumor was ulcerated.
932
933 **Adoptive cell transfers**
934 Fresh bone marrow was harvested as described in the **Bone marrow-derived macrophages**
935 **(BMDMs)** methods section. Marrow cells were counted on a hemocytometer and resuspended
936 to a concentration of $8x10^7$ cells per mL in in 5% (v/v) FBS/PBS. To block SIRPα, cells were
937 then incubated with anti-SIRPα clone P84 (18 µg/mL) for 1 h at room temperature on a rotator.
938 After the incubation period elapsed, cells were centrifuged at 300 x *g* for 5 min, washed with
939 PBS, and then centrifuged once more at 300 x *g* for 5 min to remove any unbound anti-SIRPα.
940 Cells were again re-suspended to a concentration of $8x10^7$ cells per mL in in 2% (v/v) FBS/PBS,
941 with or without anti-Tyrp1 clone TA99 (1 mg/mL). Marrow cells were then injected intravenously
942 ($2x10^7$ cells in 250 µL per mouse) into tumor-bearing mice. All adoptive transfers were done four
943 days post-challenge. Control data were adapted from (Dooling et al., 2022) to minimize mice for
944 experiments, since the cited study establishes proper benchmarks for comparison and also finds
945 that these control conditions minimally (if at all) improve survival.
946
947 **Serum collection & IgG titer quantification**
948 Blood was drawn retro-orbitally from mice anesthetized under isoflurane, using heparin- or
949 EDTA-coated microcapillary tubes. Collected blood was allowed to clot for 1 h at room
950 temperature in a microcentrifuge tube. The serum was separated from the clot by centrifugation
951 at 1,500 x *g* and stored at -20°C for use in flow cytometry and phagocytosis assays.
952
953 For IgG titer quantification, B16F10 cells were detached by trypsinization and incubated with 5%
954 (v/v) mouse serum in 1% BSA. Opsonization was allowed for 30-45 min on ice. After the
955 incubation period elapsed, cells were centrifuged at 300 x *g* for 5 min, washed once with PBS,
956 centrifuged again at 300 x *g* for 5 min, and then resuspended in 0.1% (w/v) BSA with both PE
957 anti-mouse IgG2a/c clone RMG2a-62 and APC anti-mouse IgG2b clone RMG2b-1 (see
958 **Antibodies** section for more information). Anti-IgG conjugated-antibody incubation occurred for

959 30-45 min, after which cells were centrifuged at 300 x *g* for 5 min, washed once with PBS,
960 centrifuged again at 300 x *g* for 5 min, and then resuspended in 5% (v/v) FBS/PBS. Cells were
961 run on a BD LSRII (Benton Dickinson) flow cytometer.
962
963 **Western blotting**
964 Lysate was prepared from B16F10 cells using RIPA buffer containing 1X protease inhibitor
965 cocktail (Millipore Sigma P8340) and boiled in 1X NuPage LDS sample buffer (Invitrogen
966 NP0007) with 2.5% β-mercaptoethanol. Proteins were separated by electrophoresis in NuPage
967 4-12% Bis-tris gels run with 1X MOPS buffer (Invitrogen NP0323) and transferred to an iBlot
968 nitrocellulose membrane (Invitrogen IB301002). The membranes were blocked with 5% (w/v)
969 non-fat milk in Tris buffered saline (TBS) plus Tween-20 (TBST) for 1 h and stained with 5%
970 (v/v) mouse serum overnight at 4°C with agitation. The membranes were washed TBST and
971 incubated with 1:500 secondary antibody conjugated with horseradish peroxidase (GRP) in 5%
972 (w/v) milk in TBST for 1 h at room temperature with agitation. The membranes were then washed
973 again three times with TBST. Membranes probed with HRP-conjugated secondary antibody
974 were developed a 3,3',5,5'-teramethylbenzidine (TMB) substrate (Genscript L002V or Millipore
975 Sigma T0565). Developed membranes were scanned and then processed with ImageJ.
976
977 **Immune infiltrate analysis of tumors**
978 For day 5 post-challenge measurements: If mice required anti-Tyrp1 treatment, mice received a
979 single dose of intravenously delivered anti-Tyrp1 or mouse IgG2a isotype control four days (96
980 h) post-tumor challenge. 24 later, mice were humanely sacrificed. Otherwise, mice were
981 sacrificed five days post-tumor challenge. For immune analysis of second challenge non-
982 survivors: Mice were humanely euthanized when tumor burden reached >150 mm^2.
983
984 Tumors from euthanized mice were excised and placed into 5% (v/v) FBS/PBS. Tumors were
985 then disaggregated using Dispase (Corning 354235) supplemented with 4 mg/mL of collagenase
986 type IV (Gibco 17104-019) and DNAse I (Millipore Sigma, 101041159001) for 30-45 min (until
987 noticeable disaggregation) at 37°C, centrifuged for 5 min at 300 x *g*, and resuspended in 1 mL
988 of ACK lysis buffer for 12 min at room temperature. Samples were centrifuged for 5 min at 300
989 x *g*, washed once with PBS, and then resuspended in 5% (w/v) BSA/PBS for 20 min. After 20

990 min elapsed, fluorophore-conjugated antibodies to immune markers were added to each cell
991 suspension. The following markers were used for analysis: for macrophages, CD45, CD11b,
992 F4/80, Ly-6C, Ly-6G, CD86, CD206, MHCII; for T cells, CD45, CD3e, CD8a. Antibody binding
993 occurred for 30 mins while samples were kept on ice and covered from light. Samples were then
994 centrifuged for 5 min at 300 x *g*, washed once with PBS, and resuspended in FluoroFix Buffer
995 (BioLegend, 422101) for 1 h at room temperature prior to analysis on a BD LSRII (Benton
996 Dickinson) flow cytometer. Data were analyzed with FCS Express 7 software (De Novo
997 Software).
998
999 **Bulk RNA-sequencing**
1000 RNA library was constructed using NEBNext® Ultra™ II RNA Library Prep Kit for Illumina® and
1001 NEBNext® Multiplex Oligos for Illumina (E7770S, E7335) per the manufacturer's instructions.
1002 The library prepared was processed at the Next Generation Sequencing Core at the University
1003 of Pennsylvania (12-160, Translational Research Center) using NovaSeq 6000, 100 cycles
1004 (Illumina). The reads were aligned to mouse reference, mm10 (GENCODE vM23/Ensembl 98)
1005 using star alignment. Cell count matrix was generated and imported to RStudio for downstream
1006 analysis. Package "DESeq2" (v1.32.0) was used for normalization and differential expression
1007 analysis. Package "fgsea" (v1.18.0) was used for gene set enrichment analysis. Additional
1008 exploratory data analysis was then done using either RStudio or Python 3.8.
1009
1010 **Single-cell RNA-sequencing**
1011 RNA libraries were prepared using the 10X Genomics Chromium Single Cell Gene Expression
1012 kit (v3.1, single index, PN-1000128; PN-1000127; PN-1000213) per the manufacturer's
1013 instructions. The libraries were sequenced at the Next Generation Sequencing Core using
1014 NovaSeq 6000, 100 cycles (Illumina). Raw base call (BCL) files were analyzed using CellRanger
1015 (version 5.0.1) to generate FASTQ files, and the "count" command was used to generate raw
1016 count matrices aligned to mm10 (GENCODE vM23/Ensembl 98). Cells were filtered to make
1017 sure that they expressed a minimum of 1,400 genes with less than 15 percent mitochondrial
1018 content. Data was normalized using the "LogNormalize" method from the Seurat package.
1019 Differential expression analysis was performed using the "FindAllMarkers" command, and the
1020 output was used for gene set enrichment analysis (GSEA).

1021

1022 **InferCNV**

1023 Count matrix of single cell RNA-sequencing results was used as input for InferCNV object
1024 construction (1.7.1) (InferCNV of the Trinity CTAT Project, see the following for more information:
1025 https://github.com/broadinstitute/inferCNV). Gene position files were created for GRCm38.
1026 Single-cell RNA-sequencing data of DMSO-treated B16F10 were used as reference for copy
1027 number profile construction. Cell types were annotated either manually or using the package
1028 "SingleR" (v1.6.1). For manual annotation, cells were clustered and assigned cell types based
1029 on the expression of cell type specific signature genes (SI.5a). Denoised results from InferCNV
1030 were used as the input ("infercnv.observations.txt"). The averaged copy number of each
1031 chromosome segment was calculated, and the difference between each cell's copy number and
1032 the overall mean at each segment was calculated. The deviation was summed across the entire
1033 chromosome to obtain the distribution of the deviation. Cells sharing an absolute deviation that
1034 is more than 2.5 times standard deviation away from the distribution peak were marked as
1035 outliers for a certain chromosome in question.

1036

1037 **Transcriptomic gene sets**

1038 For analyzing both bulk and single-cell RNA-sequencing data sets, either hallmark gene sets
1039 (from the Human Molecular Signatures Database) or customized gene sets were used.
1040 Customized gene sets were used exclusively for macrophage-associated analyses and were
1041 made by combining gene sets from the following: Ahn et al., 2018; Cerezo-Wallis et al., 2020;
1042 Cunha et al., 2018; Mujal et al., 2022; Perry et al., 2019; Zhou et al., 2020.

1043

1044 **Statistical analysis & curve fitting**

1045 Statistical analyses and curve fitting were performed in GraphPad Prism 9.4. Details for each
1046 analysis are provided in the figure legends. Tumor and tumoroid growth curve data (projected
1047 area vs time) were fit to the exponential growth model ($A = A_0e^{kt}$ for tumors and $A = A_1e^{k(t-1)}$ for
1048 tumoroids) using non-linear least squares regression with prefactors A_0 or A_1 and k, the
1049 exponential growth rate. For differential gene expression analysis for both bulk RNA-sequencing
1050 and single-cell RNA-sequencing datasets, statistical analyses were done using either RStudio
1051 2022.02.3+492 or Python 3.8.

1052

1053 **Code availability**

1054 Sequencing data were analyzed using RStudio 2022.02.3+492 and the Seurat package.
1055 Additional analyses after normalization were done on either RStudio or Python 3.8. No new code
1056 central to the conclusions of this study was developed.

1057

1058 **Author contributions**

1059 Conceptualization: BHH. Formal analysis: BHH, MW, HZ, SP, AC. Funding acquisition: BHH,
1060 JCA, LJD, DED. Investigation & data collection: BHH, MW, HZ, SP, AC, JCA, LJD, MPT, TM.
1061 Methodology: BHH, MW. Resources: DED. Visualization: BHH, MW. Writing: BHH, DED.

1062

1063 **Acknowledgements**

1064 This work was supported by funding from the following sources: NIH R01 HL124106 (DED), U54
1065 CA193417 (DED), NSF GRFP DGE-1845298 (BHH, JCA, MPT), and NIH F32 CA228285 (LJD).
1066 The authors acknowledge the following University of Pennsylvania core facilities: Cell Center
1067 Stockroom, the Penn Cytomics and Cell Sorting Resource Laboratory, the Penn Genomic and
1068 Sequencing Core, and the Cell & Development Biology Microscopy Core.

1069

1070 **Competing interests**

1071 The authors declare no competing interests.

1072

1073 **Data availability statement**

1074 All data are available within the article and its supplementary information. Data can be provided
1075 upon reasonable request from the corresponding author.

1076

1077 **Main Figure Legends**

1078

1079 **Figure 1. MPS1i-induced chromosomal instability causes proliferation deficits in B16F10**
1080 **tumors and generates microenvironment conditions that favor anti-cancer M1-like**
1081 **macrophages while minimizing skewing to a pro-cancer M2-like phenotype.**
1082 **(A)** Timeline and schematic for treatment of B16F10 mouse melanoma cells with MPS1 inhibitors
1083 (MPS1i). B16F10 cells were treated with MPS1i (reversine) or the equivalent volume of DMSO
1084 vehicle control. Cells were treated for 24 h, after which they were washed twice with PBS and
1085 allowed to recover for an additional 48 h. After the recovery period elapsed, numerous follow-up
1086 experiments were conducted to characterize chromosomal instability, aneuploidy, and effects
1087 on BMDMs (BMDMs).

1088

1089 **(B) (i)** Representative DNA images of B16F10 cells 72 h after initial treatment, as outlined in (A).
1090 Scale bars = 10 μm. Yellow arrowheads point at micronuclei, which are used as a signature
1091 readout of chromosomal instability. **(ii)** Quantification of the percentage of B16F10 cells with
1092 micronuclei after MPS1i treatment, across a range of different MPS1i concentrations and DMSO
1093 vehicle control (mean ± SEM shown, n = 3 replicates per condition). Statistical significance was
1094 calculated by ordinary one-way ANOVA and Tukey's multiple comparison test (* $p < 0.05$; ** $p <$
1095 0.01; *** $p < 0.001$; **** $p < 0.0001$).

1096

1097 **(C)** Inferred copy number in DMSO and MPS1i-treated B16F10 cells from single-cell RNA-
1098 sequencing and the InferCNV pipeline. Cells that are considered aneuploid (labeled as outliers
1099 in the InferCNV algorithm) show full-level chromosome gains and/or losses compared to the
1100 consensus copy number profile of the DMSO-treated B16F10 population. Approximately 34% of
1101 MPS1i-treated B16F10 show aneuploidy, as determined by InferCNV, compared to 10% in the
1102 DMSO-treated B16F10 population. Single-cell RNA-sequencing confirms that MPS1i induces
1103 chromosomal instability and aneuploidy in B16F10 cells.

1104

1105 **(D)** Timeline and schematic for whole-tumor bulk RNA-sequencing. Prior to tumor inoculation,
1106 B16F10 CD47 KO cells were treated with 2.5 μM MPS1i (reversine) or the equivalent volume of
1107 DMSO vehicle control. Cells were treated for 24 h, after which they were washed twice with PBS

and allowed to recover for an additional 48 h. After the recovery period elapsed, all mice were subcutaneously injected with $5x10^5$ B16F10 cells. Five or ten days after tumor inoculation, mice were humanely euthanized, and their tumors were excised and disaggregated for bulk RNA-sequencing analysis.

(E) Heatmap of selected RNA transcripts related to M2 macrophage polarization and pro-tumor function that were differentially expressed in tumors comprised of MPS1i-treated B16F10 compared to tumors comprised of their DMSO-treated counterpart. Heatmap shows log_2-transformed transcript reads which were then z-score normalized. Generally, M2 and pro-tumor macrophage markers are downregulated at day 5 and even further at day 10 compared to DMSO controls. Tumors analyzed were two comprised of DMSO-treated B16F10 cells five days post-inoculation, two comprised of MPS1i-treated B16F10 cells five days post-inoculation, and two comprised of MPS1i-treated B16F10 cells ten days post-inoculation.

(F) Top ten downregulated hallmark gene sets in tumors comprised of MPS1i-treated B16F10 cells (here, we consider Myc targets v1 and Myc targets v2 as one overall group). Cells from tumors made of MPS1i-treated B16F10 show downregulated transcriptional signatures of cell cycle and proliferation-related pathways, suggesting overall deficits in proliferation. Gene set enrichment analysis pathways were obtained from MSigDB. Abbreviations used: CL homeostasis = cholesterol homeostasis; OXPHOS = oxidative phosphorylation.

(G) Schema for conditioned media (secretome) treatment of BMDMs and subsequent characterization by single-cell RNA-sequencing. Media from DMSO and MPS1i-treated B16F10 cells was collected and added at a 1:1 ratio with fresh media to 7-day differentiated BMDMs (with 20 ng/mL M-CSF). Treatment was allowed for 24 h, after which BMDMs were collected and processed for single-cell RNA-sequencing.

(H) (Left) UMAP plots of expression profiles for all analyzed BMDMs, treated with the secretome from DMSO-treated (gray) or MPS1i-treated (red) B16F10 cells. Each circle represents an individual cell. **(Right)** Same UMAP plots but colors now represent cells clustered together based on similarity of global gene expression. **(Inset)** Composition of each cluster.

1139

1140 **(I)** Dot plot showing proportion of cells in each cluster expressing anti-inflammatory and M2-like
1141 polarization-associated genes (pro-cancer gene set overall). Indicated to the right are a heatmap
1142 scale for average gene expression and a dot size reference for what proportion of cells in the
1143 cluster express a gene. Clusters 1 and 3, both of which consist of ~75% of BMDMs treated with
1144 conditioned media from DMSO-treated B16F10, generally show downregulated transcript levels
1145 for genes associated with skewing macrophages to a pro-inflammatory, anti-cancer, M1-like
1146 phenotype. Cluster 3, in particular, shows significant downregulated. On the contrary, clusters 0
1147 and 2, which consist of 75% of BMDMs treated with conditioned media from MPS1i-treated
1148 B16F10, show upregulated expression of many of these anti-cancer genes. Cluster 2, in
1149 particular, shows signatures of high upregulation.

1150

1151 (**J)** Dot plot showing proportion of cells in each cluster expressing pro-inflammatory and M1-like
1152 polarization-associated genes (anti-cancer gene set overall). Indicated to the right are a heatmap
1153 scale for average gene expression and a dot size reference for what proportion of cells in the
1154 cluster express a gene. Clusters 1 and 3, both of which consist of ~75% of BMDMs treated with
1155 conditioned media from DMSO-treated B16F10, generally show upregulated transcript levels for
1156 genes associated with skewing macrophages to an anti-inflammatory, pro-cancer, M2-like
1157 phenotype. On the contrary, clusters 0 and 2, which consist of 75% of BMDMs treated with
1158 conditioned media from MPS1i-treated B16F10, show either little-to-no expression or
1159 downregulation of many of these genes.

Figure 2. Chromosomally unstable tumoroids and tumors in early stages show increased anti-cancer macrophage polarization and activity.

(A) Timeline and schematic for generating engineered "immuno-tumoroids" for time-lapsed studies of macrophage-mediated phagocytosis of cancer cells. Tumoroids are formed by plating and culturing B16F10 cells on non-adhesive surfaces in U-bottom shaped wells. Prior to plating for tumoroid formation, B16F10 were treated with either DMSO or MPS1i (reversine) as depicted in Fig. 1A. ~24 h after plating, bone marrow-derived macrophages (BMDMs) with or without opsonizing anti-Tyrp1 are added to the cohesive B16F10 tumoroids. Immuno-tumoroids are imaged at the listed timepoints. At day 5, a separate subset of prepared immuno-tumoroids were collected, dissociated, and stained for measurement of macrophage polarization markers by flow cytometry.

(B) Representative flow cytometry histograms for flow cytometry measurements of macrophage polarization markers. For M1-like (anti-tumor) markers, we chose MHCII and CD86. For M2-like (pro-tumor) markers, we chose CD163 and CD206.

(C) Geometric mean fluorescence intensity quantification by flow cytometry of anti-tumor macrophage markers (MHCII and CD86) and pro-tumor macrophage markers (CD163 and CD206) in immuno-tumoroid cultures, with either DMSO or MPS1i-treated B16F10 CD47 KO cells. Generally, immuno-tumoroid cultures with MPS1i-treated B16F10 CD47 KO cells induce surface expression of M1-like, anti-tumor markers in macrophage while also reducing expression of M2-like, pro-tumoral markers. This suggests that, in addition to reduced cancer cell proliferation, chromosomal instability in cancer cells in early stages can prime a microenvironment conducive to anti-tumor macrophages. All data were collected from five independent immune-tumoroid culture experiments (one 96-well per replicate). Statistical significance was calculated by an unpaired two-tailed t-test with Welch's correction (** $p < 0.01$).

(D) Representative fluorescence images depicting either growth or repression of B16F10 CD47 KO cells (green) in immuno-tumoroids from days 1-5. BMDMs, shown in magenta, were added at a 3:1 ratio to initial B16F10 numbers after the day 1 images were acquired. Scale bar = 0.5 mm.

1191

1192 **(E)** Tumoroid growth was measured by calculating the GFP+ area at the indicated timepoints
1193 (mean ± SD, n = 16 total tumoroids from two independent experiments for each condition). All
1194 data were then normalized to average GFP+ area on day 1 of each drug treatment's respective
1195 mouse IgG2a isotype control condition. Overall, macrophages can clear MPS1i-treated B16F10
1196 cells regardless of either MPS1i treatment concentration or IgG opsonization.

1197

1198 **(F)** Experimental timeline for immune cell infiltration analyses in tumors comprised of either
1199 DMSO or MPS1i-treated B16F10 CD47 KO cells. Prior to tumor inoculation, B16F10 CD47 KO
1200 cells were treated with 2.5 μM MPS1i (reversine) or the equivalent volume of DMSO vehicle
1201 control. Cells were treated for 24 h, after which they were washed twice with PBS and allowed
1202 to recover for an additional 48 h. After the recovery period elapsed, all C57BL/6 mice were
1203 subcutaneously injected with $2x10^5$ B16F10 cells. Four days (96 h) post-challenge, mice were
1204 treated with 250 μg of anti-Tyrp1 or mouse IgG2a isotype. Mice were then euthanized 24 h after
1205 antibody treatment, and their tumors were excised and disaggregated for immune infiltrate
1206 analysis by flow cytometry.

1207

1208 **(G)** Immune cell infiltrate measurements of B16F10 CD47 KO tumors comprised of DMSO or
1209 MPS1i-treated cells. **(i)** Quantification of the percentage of CD45+ (immune) cells in the excised
1210 tumors, showing that tumors comprised of MPS1i-treated cells show ~3-fold increased tumor
1211 immune cell infiltrate compared to their DMSO counterparts. **(ii)** Quantification of the percentage
1212 of tumor infiltrating myeloid cells in the excised tumors. B16F10 CD47 KO tumors comprised of
1213 MPS1i-treated cells show ~2.5-fold more myeloid cells compared to their DMSO counterparts.
1214 **(iii)** Quantification of tumor infiltrating F4/80+ macrophages relative to the total number of tumor
1215 cells, with the tumors comprised of MPS1i-treated cells showing a ~6-fold increase compared to
1216 their DMSO counterparts. **(iv)** Quantification of the number of M1-like macrophages
1217 ($CD86^{hi}CD206^{lo}$) and M2-like macrophages ($CD86^{lo}CD206^{hi}$) relative to the total number of
1218 macrophages in each tumor condition. Tumors comprised of MPS1i-treated cells have ~6-fold
1219 more $CD86^{hi}CD206^{lo}$ compared to their DMSO counterparts. They also have a similar increase
1220 in $CD86^{lo}CD206^{hi}$ macrophages, but the number of $CD86^{hi}CD206^{lo}$ macrophages was still overall
1221 twice as high. Mean ± SEM shown (n = 8 mice challenged with DMSO-treated B16F10 cells, n

1222 = 5 mice challenged with MPS1i-treated B16F10 cells). Statistical significance was calculated
1223 by an unpaired two-tailed t-test with Welch's correction (ns, not significant; ** $p < 0.01$; **** $p <$
1224 0.0001).
1225
1226
1227
1228

1229 **Figure 3. MPS1i-induced chromosomally unstable cancer cells are maximally cleared**
1230 **when IgG-opsonized and depleted of the CD47 macrophage checkpoint.**
1231 **(A**) Timeline for *in vitro* treatment B16F10 cells prior to injection in mice and then subsequent
1232 therapeutic treatment for tumor-challenged mice. Prior to tumor inoculation, B16F10 CD47 KO
1233 cells were treated with 2.5 μM MPS1i (reversine) or the equivalent volume of DMSO vehicle
1234 control. Cells were treated for 24 h, after which they were washed twice with PBS and allowed
1235 to recover for an additional 48 h. After the recovery period elapsed, all mice were subcutaneously
1236 injected with $2x10^5$ B16F10 cells. For anti-Tyrp1 and mouse IgG2a isotype control treatments,
1237 mice were treated intravenously or intraperitoneally with 250 μg with antibody on days 4, 5, 7, 9,
1238 11, 13, and 15 after tumor challenge.
1239
1240 **(B)** Tumor growth curve of projected tumor area versus days after tumor challenge, with B16F10
1241 sgCtrl cells (expressing WT levels of CD47). Each line represents a separate tumor and is fit
1242 with an exponential growth equation: $A = A_0e^{kt}$. Experimental conditions are as follows: n = 9
1243 mice that were challenged with DMSO-treated B16F10 sgCtrl and subsequently treated with
1244 mouse IgG2a control, n = 11 mice that were challenged with DMSO-treated B16F10 sgCtrl and
1245 subsequently treated with anti-Tyrp1, n = 6 mice that were challenge with MPS1i-treated B16F10
1246 sgCtrl and subsequently treated with mouse IgG2a control, and n = 7 mice that were challenge
1247 with MPS1i-treated B16F10 sgCtrl and subsequently treated with anti-Tyrp1. All data were
1248 collected across three independent experiments. Inset bar graphs depict response type for each
1249 indicated tumor challenge. A partial response was defined as a mouse that survived at least one
1250 week (20+ days) beyond the median survival of the B16F10 sgCtrl cohort treated with mouse
1251 IgG2a isotype control (13 days).
1252
1253 **(C)** Tumor growth curve of projected tumor area versus days after tumor challenge, with B16F10
1254 CD47 KO cells. Each line represents a separate tumor and is fit with an exponential growth
1255 equation: $A = A_0e^{kt}$. Complete anti-tumor responses in which a tumor never grew are depicted
1256 with the same symbol as their growing counterparts and with solid lines at A = 0. Experimental
1257 conditions are as follows: n = 7 mice that were challenged with DMSO-treated B16F10 CD47
1258 KO and subsequently treated with mouse IgG2a control, n = 9 mice that were challenged with
1259 DMSO-treated B16F10 CD47 KO and subsequently treated with anti-Tyrp1, n = 14 mice that

1260 were challenge with MPS1i-treated B16F10 CD47 KO and subsequently treated with mouse
1261 IgG2a control, and n = 35 mice that were challenge with MPS1i-treated B16F10 CD47 KO and
1262 subsequently treated with anti-Tyrp1. All data in which mice were challenged with DMSO-treated
1263 cells were collected from three independent experiments. Data for the condition in which mice
1264 were challenged with MPS1i-challenged cells and then given mouse IgG2a control were
1265 collected from four independent experiments. Data for the final condition in which mice were
1266 injected with MPS1i-treated cells and then treated with anti-Tyrp1 was collected from seven
1267 independent experiments. Inset bar graphs depict response type for each indicated tumor
1268 challenge. A partial response was defined as a mouse that survived at least one week (20+
1269 days) beyond the median survival of the B16F10 sgCtrl cohort treated with mouse IgG2a isotype
1270 control (13 days).
1271
1272 **(D)** Survival curves of mice up to 100 days after the tumor challenges in (B) and (C). **(i)** Survival
1273 curves for mice challenged with B16F10 sgCtrl. **(ii)** Survival curves for mice challenged with
1274 B16F10 CD47 KO. **(iii)** Triangular matrix depicting p-values between the different tested *in vivo*
1275 conditions. Statistical significance was determined by the Log-rank (Mantel-Cox) test.
1276
1277 **(E) (i)** Schematic depicting the different engineering anti-tumor macrophage strategies that can
1278 be used for validating macrophages' role in clearing CIN-afflicted B16F10 cells. Fresh bone
1279 marrow was isolated from the tibia of donor C57BL/6 mice and was then incubated with anti-
1280 SIRPα clone P84 (18 μg/mL) or anti-Tyrp1 (1 μg/mL) only, both together added subsequently,
1281 or neither. Donor marrow ($2x10^7$ cells) is then injected intravenously into C57BL/6 harboring
1282 B16F10 WT tumors on day 4 post-challenge. Additional anti-Tyrp1 injections, when necessary,
1283 are done on days 5, 7, 9, 11, 13, and 15 post-tumor challenge. **(ii)** Survival curves of mice up to
1284 100 days after the B16F10 WT tumor challenge. All mice were initially challenged with $2x10^5$
1285 B16F10 WT cells. **(iii)** Triangular matrix depicting p-values between the different tested *in vivo*
1286 conditions. Statistical significance was determined by the Log-rank (Mantel-Cox) test.
1287

1288 **Figure 4. MPS1i-induced chromosomal instability favors induction of pro-phagocytic *de***
1289 ***novo* IgG and can lead to durable acquired immunity.**
1290 **(A)** Schematic illustrating protocol for sera collection from surviving mice from Fig. 3C-D and
1291 follow-up experiments to characterize potential *de novo* anti-cancer IgG antibodies and their
1292 functionality both *in vitro* and *in vivo*. Serum from all mice was collected at least 100 days after
1293 initial tumor challenge.
1294
1295 **(B) (i)** Representative flow cytometry histograms showing that convalescent sera from survivors
1296 in Fig. 3C-D contain IgG2a/c (top) and IgG2b (bottom) that bind to both WT and Tyrp1 KO
1297 B16F10 cells.
1298
1299 **(ii)** Median fluorescence intensity quantification of IgG2a/c and IgG2b binding from sera from
1300 surviving mice. Convalescent sera show statistically significant increase in both IgG2a/c and
1301 IgG2b titers. Binding to even Tyrp1 KO cells suggests broader recognition of antigens unique to
1302 B16F10. Statistical significance was calculated by an unpaired two-sample Kolmogorov-Smirnov
1303 test (**** $p < 0.0001$). For IgG2a/c quantification: for binding against Tyrp1+ cells, n = 23 distinct
1304 naïve serum samples and n = 28 distinct convalescent serum samples from surviving mice; for
1305 binding against Tyrp1 KO cells, n = 23 distinct naïve serum samples and n = 27 distinct
1306 convalescent serum samples. For IgG2b quantification: for binding against Tyrp1+ cells, n = 14
1307 distinct naïve serum samples and n = 16 distinct convalescent serum samples from surviving
1308 mice; for binding against Tyrp1 KO cells, n = 13 distinct naïve serum samples and n = 17 distinct
1309 convalescent serum samples.
1310
1311 **(iii)** Western blotting of B16F10 lysate with either naïve sera or first challenge survivor sera as
1312 primary probe followed by anti-mouse IgG [H+L] secondary staining. Numerous bands appear
1313 when immunoblotting with convalescent survivor sera (and more than when immunoblotting with
1314 naïve sera), qualitatively confirming binding to numerous antigens and suggesting acquired
1315 immunity beyond Tyrp1.
1316
1317 **(C) (i)** Phagocytosis of serum-opsonized CD47 KO or CD47/Tyrp1 double KO B16F10 cells by
1318 BMDMs on 2D tissue culture plastic. Additionally, B16F10 cells opsonized with either anti-Tyrp1

or mouse IgG2a were included as controls for comparisons. Serum IgG derived from survivors has both opsonization and pro-phagocytic functional ability against B16F10. Furthermore, convalescent sera IgG from survivors is still able to drive engulfment of Tyrp1 KO cells, further suggesting targeting of antigens beyond Tyrp1. Statistical significance was calculated by two-way ANOVA and Tukey's multiple comparison test (mean ± SD, n = 21-23 distinct sera samples collected from survivors for B16F10 CD47 KO phagocytosis per condition and n = 14-23 for B16F10 CD47/Tyrp1 double KO phagocytosis per condition).

(ii) Convalescent sera from first challenge survivors can repress growth of B16F10 CD47 KO immuno-tumoroids (with macrophages). Tumoroid growth was measured by calculating the GFP+ area at the indicated timepoints (mean ± SD, n = 16 total tumoroids from two independent experiments for each condition, except n = 8 for opsonization with sera from naïve mice). Statistical significance was calculated by Brown-Forsythe and Welch ANOVA tests with Dunnett T3 corrections for multiple comparisons (ns, not significant; ** $p < 0.01$; **** $p < 0.0001$). Scale bars = 0.5 mm.

(D) B16F10 CD47 KO cells were pre-opsonized with either convalescent sera from first challenge survivors, anti-Tyrp1 or mouse IgG2a isotype control. All mice were subcutaneously injected with $2x10^5$ pre-opsonized B16F10 CD47 KO cells.

(i) Tumor growth curves shown are at early timepoints where growth is still in the linear regime. Linear fits highlight growth suppression of tumors comprised of B16F10 CD47 KO cells pre-opsonized with convalescent sera and anti-Tyrp1, compared to the mouse IgG2a isotype counterparts. Mean ± SEM for all timepoints, with n = 16 mice with tumors pre-opsonized with convalescent sera (each from a distinct survivor), n = 9 mice with tumors pre-opsonized with anti-Tyrp1, and n = 14 mice with tumors pre-opsonized with mouse IgG2a isotype control. Statistical significance was calculated by ordinary one-way ANOVA and Tukey's multiple comparison test at days 9, 11, and 13 (* $p < 0.05$; **** $p < 0.0001$). Significance represented in plot legend is representative of all three timepoints.

1349 **(ii)** Survival curves up to 100 days of mice from (D-i) with pre-opsonized tumors. Both
1350 convalescent sera and anti-Tyrp1 provide similar survival benefits, suggesting potent *de novo*
1351 IgG opsonization and anti-cancer function. Statistical significance was determined by the Log-
1352 rank (Mantel-Cox) test (ns, not significant; ** $p < 0.01$; **** $p < 0.0001$).
1353
1354 **(E)** Schematic illustrating the series of experimental tumor challenges to assess acquired
1355 immunity. Survivors from the first challenge (Fig. 3C-D) were again challenged with either DMSO
1356 or MPS1i-treated B16F10 CD47 KO cells. Survivors from this second tumor challenge were once
1357 again challenged, this time with untreated B16F10 CD47 KO.
1358
1359 **(F)** Survival curves of survivors from Fig. 3C-D for a second tumor challenge experiment. Prior
1360 to tumor inoculation, B16F10 CD47 KO cells were treated with 2.5 μM MPS1i (reversine) or the
1361 equivalent volume of DMSO vehicle control. Cells were treated for 24 h, after which they were
1362 washed twice with PBS and allowed to recover for an additional 48 h. After the recovery period
1363 elapsed, all mice were subcutaneously injected with $2x10^5$ B16F10 CD47 KO cells. Experimental
1364 conditions are as follows: n = 7 age-matched naïve mice (never tumor-challenged) injected with
1365 DMSO-treated B16F10 CD47 KO cells, n = 11 surviving mice (from Fig. 3C-D) injected DMSO-
1366 treated B16F10 CD47 KO cells, n = 6 age-matched naïve mice injected with MPS1i-treated
1367 B16F10 CD47 KO cells, and n = 8 surviving mice (from Fig. 3C-D) injected with MPS1i-treated
1368 B16F10 CD47 KO cells. Previous survivors challenged with DMSO-treated B16F10 CD47 KO
1369 cells show increased median survival (21 days) compared to their naïve counterpart (14 days).
1370 All previous survivors that were again challenged with MPS1i-treated B16F10 CD47 KO cells
1371 survive. All mice challenged were from three independent experiments. Statistical significance
1372 was determined by the Log-rank (Mantel-Cox) test (** $p < 0.01$; *** $p < 0.001$; **** $p < 0.0001$).
1373
1374 **(G)** Non-survivors from the second tumor challenge in (F) were euthanized after tumor size was
1375 >150 mm^2, and their tumors were excised and disaggregated for immune infiltrate analysis by
1376 flow cytometry. **(i)** Quantification of CD45+ (immune) cells in the excised tumors, showing that
1377 first challenge survivors still show ~2.5-fold increased tumor immune cell infiltrate despite
1378 reaching terminal burden. n = 4 mice for age-matched naïve control, n = 5 mice that survived
1379 the first tumor challenge. **(ii)** Quantification of tumor infiltrating CD8a+ cytotoxic T cell relative to

1380 the total number of tumor cells. First challenge survivors show ~2-fold increase in CD8a+ T cells.
1381 n = 4 mice for age-matched naïve control, n = 3 mice that survived the first tumor challenge. **(iii)**
1382 Quantification of tumor infiltrating F4/80+ macrophages relative to the total number of tumor
1383 cells. First challenge survivors show ~3-fold increase in macrophages. n = 4 mice for age-
1384 matched naïve control, n = 5 mice that survived the first tumor challenge. **(iv)** Quantification of
1385 MHCII+ tumor infiltrating F4/80+ macrophages relative to the total number of F4/80
1386 macrophages. First challenge survivors show ~3-fold increase in MHCII+ macrophages. n = 4
1387 mice for age-matched naïve control, n = 5 mice that survived the first tumor challenge. For all
1388 experiments, mean ± SEM shown, and statistical significance was calculated by an unpaired
1389 two-tailed t-test with Welch's correction (* $p < 0.05$; ** $p < 0.01$; *** $p < 0.001$; **** $p < 0.0001$).
1390
1391 **(H) (i)** Third tumor challenge survival curves of long-term survivors from (G). All mice were
1392 challenged with $2x10^5$ B16F10 CD47 KO cells (n = 9 mice from three independent experiments),
1393 delivered subcutaneously. For benchmarking and statistical comparison, survival curves from
1394 Fig. 3F for naïve mice (n = 7 mice from three independent experiments) and second challenge
1395 (n = 11 mice from three independent experiments) are included. Long-term survivors challenged
1396 a third time show ~70% survival without any additional therapeutic modality, suggesting
1397 significantly improved acquired immune response. Statistical significance was determined by the
1398 Log-rank (Mantel-Cox) test (** $p < 0.01$; *** $p < 0.001$; **** $p < 0.0001$).
1399
1400 **(ii)** Individual tumor growth curves for third challenge in long-term survivors (n = 9 mice from
1401 three independent experiments) shown in (H-i). In total, 4 mice developed tumors, two of which
1402 had to be euthanized prematurely due to tumor rupture despite not reach a terminal burden of
1403 125 mm^2. These mice are still considered and included as casualties in the survival curve
1404 analysis. The two remaining mice show significantly slower tumor growth than naïve mice
1405 challenged with regular B16F10 CD47 KO (median survival of 14 days) and can be considered
1406 durable partial responders.
1407

1408 **Supplementary Figure Legends**

1409

1410 **Supplementary Figure 1. Characterization of MPS1i-induced genome and chromosomal**
1411 **instability in B16F10 mouse melanoma.**

1412 **(A)** Quantification of micronuclei induced by different MPS1 inhibitors (AZ3146, BAY 12-17389,
1413 and reversine) at different concentrations. Statistical significance was calculated by ordinary
1414 one-way ANOVA and Tukey's multiple comparison test (* $p < 0.05$; ** $p < 0.01$; *** $p < 0.001$;
1415 **** $p < 0.0001$).

1416 **(B)** Consensus clustering of B16F10 analyzed in single-cell RNA-sequencing. B16F10 cells
1417 were treated with 2.5 μM MPS1i (reversine) or the equivalent volume of DMSO vehicle control.
1418 Cells were treated for 24 h, after which they were washed twice with PBS and allowed to recover
1419 for an additional 48 h. Cells were then collected and processes using 10X Genomics Chromium
1420 Single Cell Gene Expression kit for RNA isolation and library preparation.

1421 **(C) (i)** UMAP plots of expression profiles for all B16F10 analyzed in single-cell RNA-sequencing.
1422 Top: UMAP plots depict clusters in which B16F10 fall, as determined by consensus clustering.
1423 Bottom: UMAP plots highlight cells with detectable copy number variations (CNVs), as
1424 determined by InferCNV. Red circles indicate individual cells with at least one CNV. Gray circles
1425 represent individual cells with no detectable CNV, suggesting these are chromosomally stable.
1426 **(ii)** Quantification of the composition (MPS1i-treated or DMSO-treated B16F10) of each cluster.

1427

1428 **Supplementary Figure 2. Characterization of MPS1i-induced genome and chromosomal**
1429 **instability in B16F10 mouse melanoma.**

1430 **(A)** Flow cytometry analysis of CD47 and Tyrp1 expression on B16F10 mouse melanoma cells.
1431 Representative histograms for anti-CD47 (left) and anti-Tyrp1 (right) binding to B16F10 CD47
1432 knockout (KO) and sgRNA ctrl (wild-type CD47 expression). Binding was detected by using
1433 secondary antibodies conjugated with Alexa Fluor 647.

1434 **(B)** Phagocytosis of B16F10 cells in in a standard phagocytosis assay on two-dimensional tissue
1435 culture plastic, with or without the following: IgG opsonization by anti-Tyrp1, CD47 KO, and
1436 MPS1i-treatment of B16F10. B16F10 cells were treated with MPS1i or DMSO prior to this assay,
1437 following the same protocol described in Fig. 1A. **(i)** Schematic of the 2D phagocytosis assay.
1438 **(ii)** Representative images of phagocytosis. B16F10 cells (green) were incubated with

1439 opsonizing anti-Tyrp1 or mouse IgG2a control and added to adherent bone marrow-derived
1440 macrophages (magenta). Random fields were imaged and then quantified to determine the
1441 percentage of phagocytic macrophages. Yellow arrowheads denote phagocytic events
1442 (complete engulfment of a target B16F10 cells). **(iii)** Quantification of phagocytic macrophages.
1443 Statistical significance was calculated by three-way ANOVA and Tukey's multiple comparison
1444 test. Mean ± SD shown, n = 3 replicates per condition (** $p < 0.01$; **** $p < 0.0001$).
1445 **(C)** Quantification of cell size measurements by flow cytometry in both MPS1i- and DMSO-
1446 treated cells. Statistical significance was calculated by three-way ANOVA and Tukey's multiple
1447 comparison test. Mean ± SD shown, n = 3 replicates per condition (* $p < 0.05$; ** $p < 0.01$; *** p
1448 < 0.001).
1449 **(D)** Quantification of Tyrp1 expression by flow cytometry in both MPS1i- and DMSO-treated
1450 cells. Statistical significance was calculated by three-way ANOVA and Tukey's multiple
1451 comparison test. Mean ± SD shown, n = 3 replicates per condition (**** $p < 0.0001$).
1452 **(E)** Quantification of CD47 expression by flow cytometry in both MPS1i- and DMSO-treated
1453 B16F10 sgCtrl cells. Statistical significance was calculated by three-way ANOVA and Tukey's
1454 multiple comparison test. Mean ± SD shown, n = 3 replicates per condition (**** $p < 0.0001$).
1455
1456 **Supplementary Figure 3. Macrophages readily clear CIN-afflicted tumoroids but only if**
1457 **CIN is accompanied by proliferation deficits.**
1458 **(A**) Timeline and schematic for generating engineered "immuno-tumoroids" for time-lapsed
1459 studies of macrophage-mediated phagocytosis of cancer cells. Tumoroids are formed by plating
1460 and culturing B16F10 cells on non-adhesive surfaces in U-bottom shaped wells. Prior to plating
1461 for tumoroid formation, B16F10 were treated with either MPS1i or DMSO (AZ3146, BAY 12-
1462 17389 or reversine). Tumoroid growth was measured by calculating the GFP+ area at the
1463 indicated timepoints (mean ± SD, n = 16 total tumoroids from two independent experiments for
1464 each condition). All data were then normalized to average GFP+ area on day 1 of each drug
1465 treatment's respective mouse IgG2a isotype control condition. Immuno-tumoroids are imaged at
1466 the listed timepoints. **(B)** To assess macrophage-mediated clearance, ~24 h after plating, bone
1467 marrow-derived macrophages (BMDMs) with or without opsonizing anti-Tyrp1 are added to the
1468 cohesive B16F10 tumoroids. Tumoroid growth curves for DMSO-treated B16F10 CD47
1469 knockout (KO) cells. **(C)** Tumoroid growth curves (with BMDMs) for MPS1i-treated B16F10

1470 CD47 KO cells (treated with varying concentrations of MPS1i): **(i)** AZ3146, **(ii)** BAY 12-17389.
1471 **(D)** Tumoroid growth curves (without BMDMs) for MPS1i-treated B16F10 CD47 KO cells (treated
1472 with varying concentrations of MPS1i): **(i)** BAY 12-17389, **(ii)** reversine. Both BAY 12-17389 and
1473 reversine induce proliferation deficits, which may play an essential role in mediating clearance
1474 by macrophages that could not be observed in AZ3146-treated cells.
1475
1476 **Supplementary Figure 4. MPS1i-induced chromosomal instability upregulates MHC-1**
1477 **class molecules on B16F10, suggesting increased antigen presentation.**
1478 Flow cytometry analysis and quantification H-2K^b expression on B16F10 mouse melanoma cells.
1479 B16F10 cells were treated with MPS1i or the equivalent volume of DMSO vehicle control.
1480 Concentrations used: 2.5 μM AZ3146, 1.0 μM BAY 12-17380, and 2.5 μM reversine. Cells were
1481 treated for 24 h, after which they were washed twice with PBS and allowed to recover for an
1482 additional 48 h. Binding was detected by using primary antibodies conjugated with Alexa Fluor
1483 647. Statistical significance was calculated by Brown-Forsythe and Welch ANOVA and Dunnett's
1484 T3 multiple comparison test. Mean ± SEM shown, n = 3 independent replicates (* $p < 0.05$; ** p
1485 < 0.01; *** $p < 0.001$; **** $p < 0.0001$).
1486
1487 **Supplementary Figure 5. Flow cytometry gating strategy for identification & quantification**
1488 **of macrophage infiltrate and characterization in CIN-afflicted and chromosomally stable**
1489 **B16F10 tumors.**
1490 Representative flow cytometry gating strategy for *in vivo* B16F10 CD47 KO tumor immune
1491 infiltrate five days after initial challenge. Tumors were comprised of cells treated with either **(i)**
1492 DMSO or **(ii)** MPS1i (2.5 μM), following the timeline schema in Fig. 2F. Singlets were separated
1493 from debris, doublets, and aggregates by FSC-A vs FSC-H and SSC-A vs SSC-H gates. Debris
1494 and dead cells were further removed by FSC-A vs SSC-A gating. Overall immune cell infiltrate
1495 was determined by CD45+ expression. Macrophages were then further identified based on
1496 Ly6G- and F4/80+ expression. Upon identification of macrophages, cells were further
1497 characterized for polarization based on CD86 (M1-like marker) and CD206 (M2-like marker)
1498 expression.
1499

1500 **Supplementary Figure 6. MPS1i-induced CIN favors clearance when paired with CD47 KO**
1501 **and IgG opsonization, regardless of the degree of CIN.**
1502 Tumor growth curve of projected tumor area versus days after tumor challenge, with B16F10
1503 CD47 KO cells. Each line represents a separate tumor and is fit with an exponential growth
1504 equation: $A = A_0e^{kt}$. Complete anti-tumor responses in which a tumor never grew are depicted
1505 with the same symbol as their growing counterparts and with solid lines at A = 0.
1506 **(A**) Tumor growth curve data in which there was no complete response, from Fig. 3C. n = 7 mice
1507 that were challenged with DMSO-treated B16F10 CD47 KO and subsequently treated with
1508 mouse IgG2a control, n = 9 mice that were challenged with DMSO-treated B16F10 CD47 KO
1509 and subsequently treated with anti-Tyrp1.
1510 **(B)** Tumor growth curve data from mice challenges with CIN-afflicted B16F10, but with varying
1511 concentration of MPS1i used to cause different degrees of instability. All mice here were
1512 challenged with B16F10 CD47 KO and treated with anti-Tyrp1 for conditions of maximal
1513 phagocytosis and to better compare to the ~97% cure rate in Fig. 3C, 4D-ii. n = 6 mice challenged
1514 with cells with each tested MPS1i concentration: 0.1, 0.5, 1.0 or 2.5 μM.
1515 **(C)** Survival curves of mice up to 100 days after the tumor challenges in (A) and (B).
1516
1517 **Supplementary Figure 7. Survivors challenged with CIN-afflicted tumors generate anti-**
1518 **cancer IgG, regardless of the degree of CIN.**
1519 Median fluorescence intensity quantification of IgG2a/c and IgG2b binding from sera from
1520 surviving mice with different degrees of chromosomal instability by titrating reversine
1521 concentration used to treat B16F10 CD47 KO cells before injection. Convalescent sera are
1522 collected from survivors from Fig. S6. Binding of IgG2a/c and IgG2b against **(A)** B16F10 cells
1523 expressing Tyrp1 and **(B)** B16F10 Tyrp1 knockout (KO). n = 4-5 distinct sera samples collected
1524 from survivors.
1525
1526 **Supplementary Figure 8. Flow cytometry gating strategy for identification & quantification**
1527 **of immune infiltrate and characterization in re-challenge experiments.**
1528 Representative flow cytometry gating strategy for *in vivo* B16F10 CD47 KO tumor immune
1529 infiltrate from 2nd challenge non-survivors and age-matched naïve controls. Singlets were
1530 separated from debris, doublets, and aggregates by FSC-A vs FSC-H and SSC-A vs SSC-H

1531 gates. Debris and dead cells were further removed by FSC-A vs SSC-A gating. For T cell
1532 quantification: CD45+ cells were gated on and then analyzed for CD3e and CD8a surface protein
1533 expression. For macrophage quantification: myeloid cells were isolated by CD45+ and CD11b+
1534 expression, after which macrophages were isolated based on F4/80 expression.
1535
1536
1537

Figure 1

MPS1i-induced chromosomal instability & deficits in proliferation favor pro-inflammatory macrophages

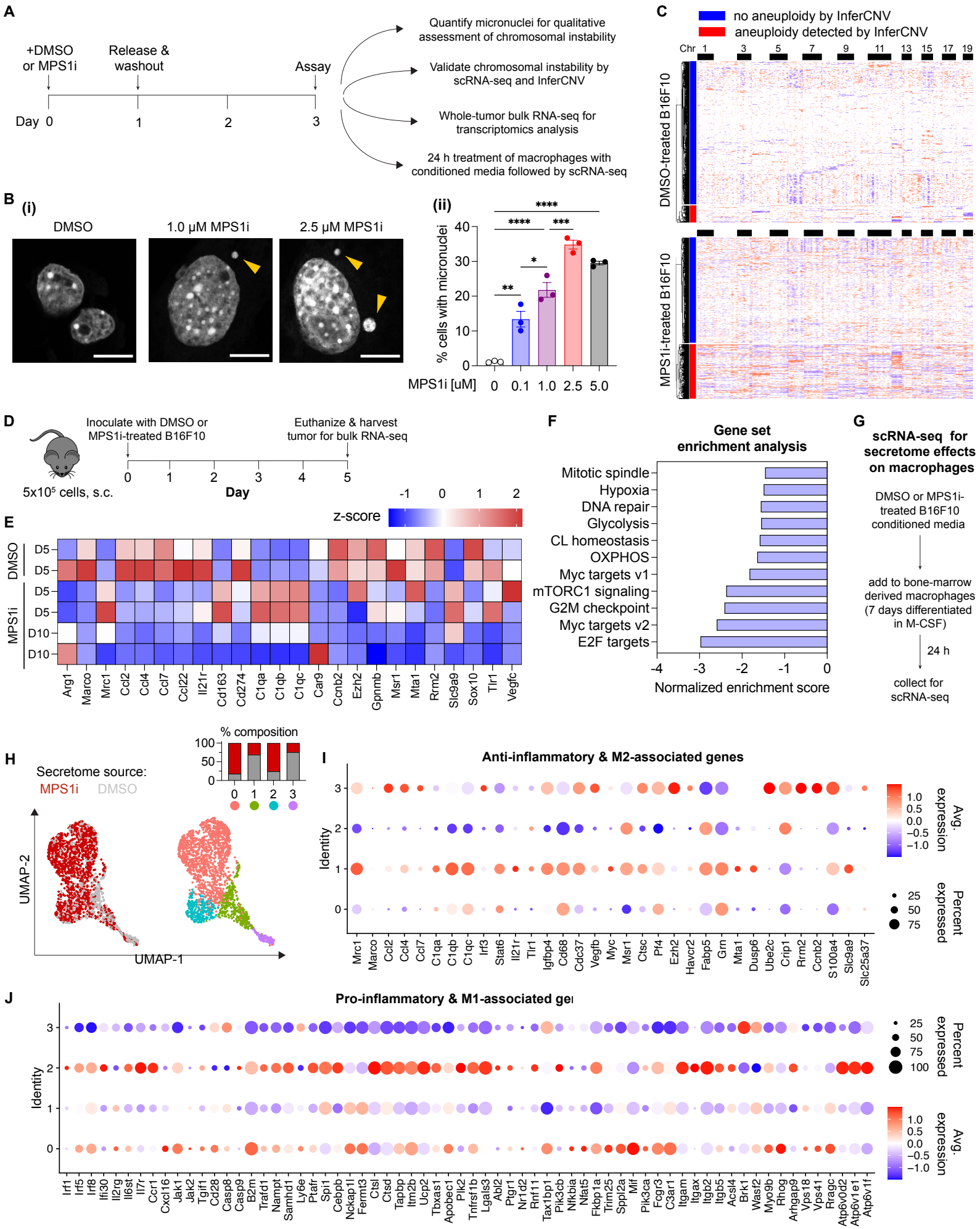

Figure 2

Macrophages readily clear genomically unstable tumoroids & skew to an M1-like phenotype

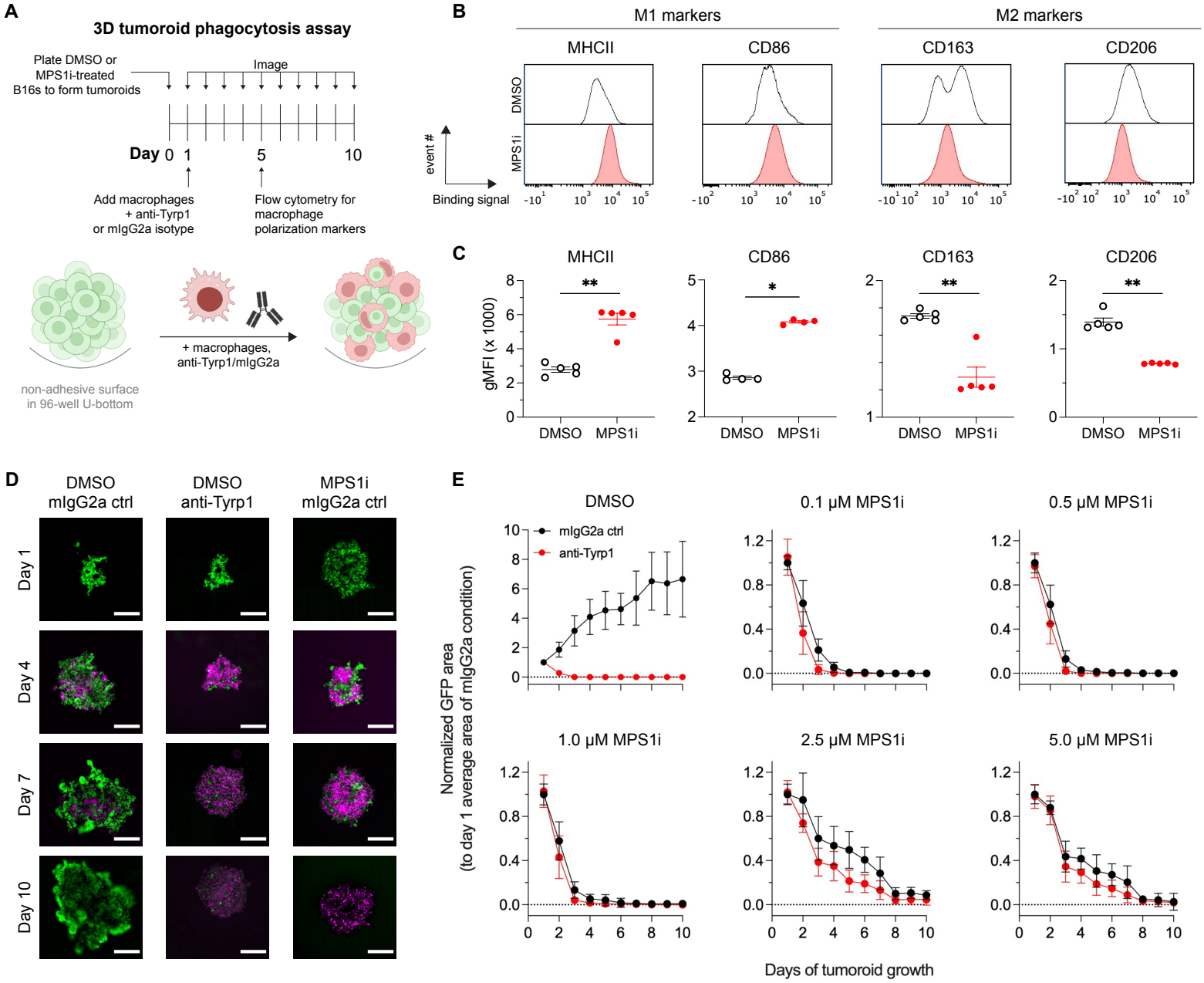

Genomically unstable tumors show increased immune infiltrate & particularly greater macrophage numbers at early stages of engraftment

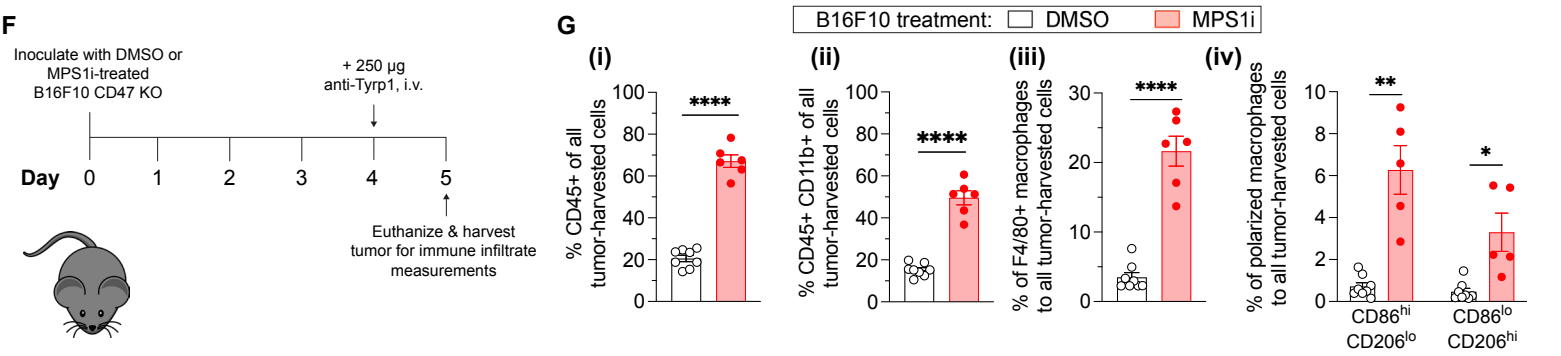

Figure 3

MPS1i-treated cancer cells are maximally cleared when IgG-opsonized & depleted of the CD47 macrophage checkpoint

A

***In vitro* drug treatment prior to injection**

Hours 0 — +DMSO or MPS1i *in vitro*

24 — Release & washout

48

72 — Detach & prepare B16F10 for inoculation

$2x10^5$ cells, s.c.

Day 0 — 4 5 7 9 11 13 15

anti-Tyrp1 or mIgG2a injections at indicated days

***In vivo* treatment scheme**

B **B16F10 sgCtrl:**

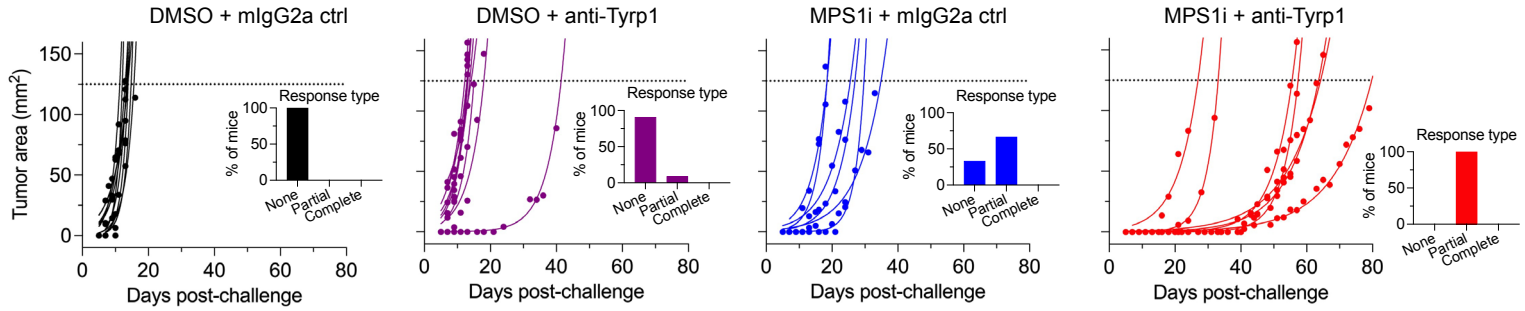

C **B16F10 CD47 KO:**

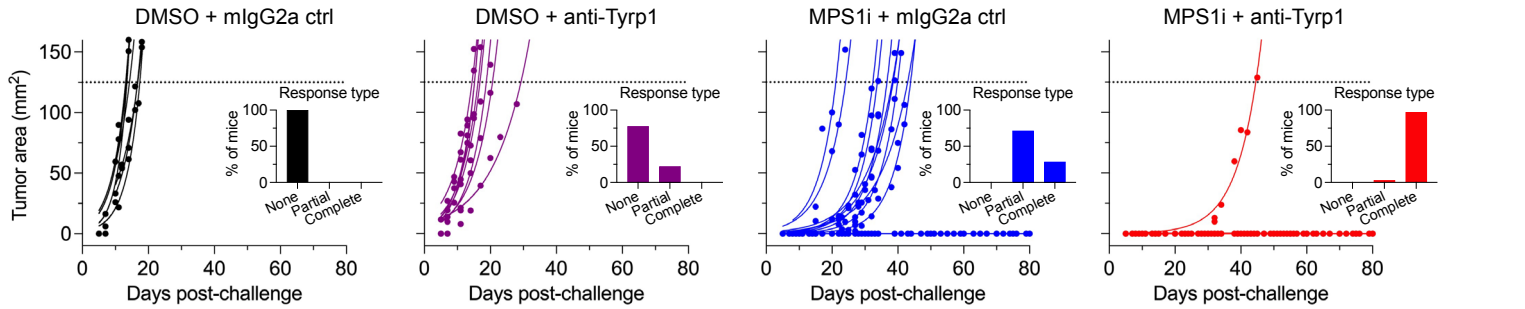

D (i)

B16F10 sgCtrl	Opsonin	Survivors
DMSO	mIgG2a	0/9
DMSO	anti-Tyrp1	0/11
MPS1i	mIgG2a	0/6
MPS1i	anti-Tyrp1	0/7

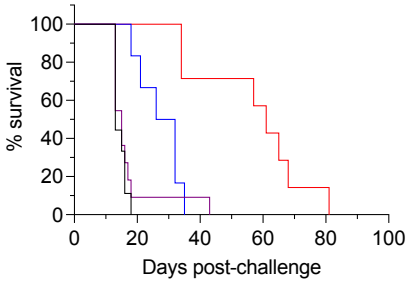

(ii)

B16F10 CD47 KO	Opsonin	Survivors
DMSO	mIgG2a	0/7
DMSO	anti-Tyrp1	0/9
MPS1i	mIgG2a	4/14
MPS1i	anti-Tyrp1	34/35

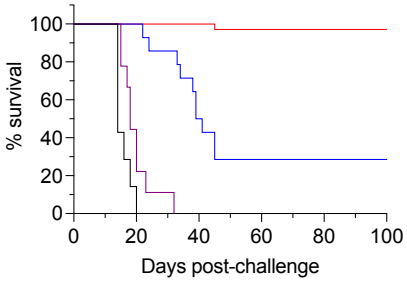

(iii)

	MPS1i	anti-Tyrp1	sgCtrl	CD47 KO	sgCtrl	CD47 KO	sgCtrl	CD47 KO
sgCtrl	—	+	0.5090					
sgCtrl	+	—	0.0004	0.0628				
sgCtrl	+	+	0.0001	0.0002	0.0017			
CD47 KO	—	—	0.2041	0.7730	0.0013	0.0001		
CD47 KO	—	+	0.0030	0.1456	0.0372	0.0001	0.0499	
CD47 KO	+	—	0.0001	0.0001	0.0008	0.8405	0.0001	0.0001
CD47 KO	+	+	0.0001	0.0001	0.0001	0.0001	0.0001	0.0001

Adoptive marrow transfer shows that increased macrophage numbers can circumvent inhibitory CD47 signaling in chromosomally unstable wild-type tumors

E (i)

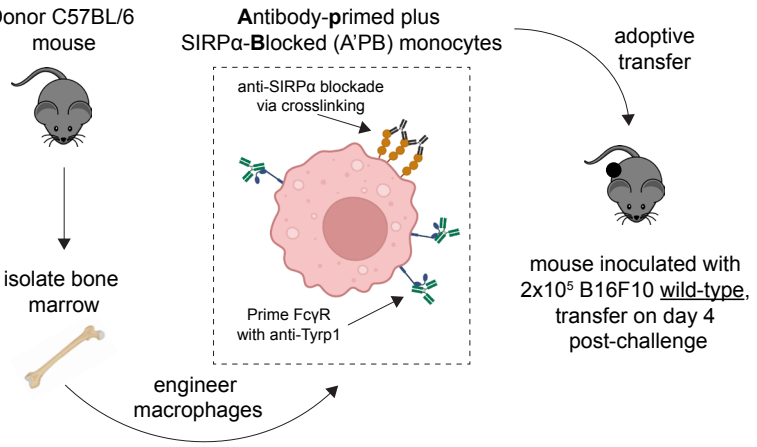

(ii)

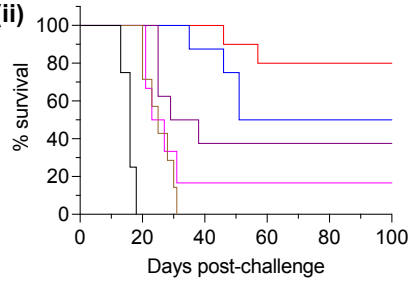

	Survivors
DMSO	0/4
DMSO + anti-SIRPα + anti-Tyrp1	1/6
MPS1i	1/7
MPS1i + anti-SIRPα	3/8
MPS1i + anti-Tyrp1	4/8
MPS1i + anti-SIRPα + anti-Tyrp1	8/10

(iii)

0.0013				
0.0006	0.5042			
0.0003	0.2005	0.0321		
0.0003	0.0192	0.0001	0.2972	
0.0001	0.0015	0.0001	0.0327	0.1636

Figure 4

Surviving chromosomally unstable tumors leads to a broad *de novo* pro-phagocytic & anti-cancer IgG response

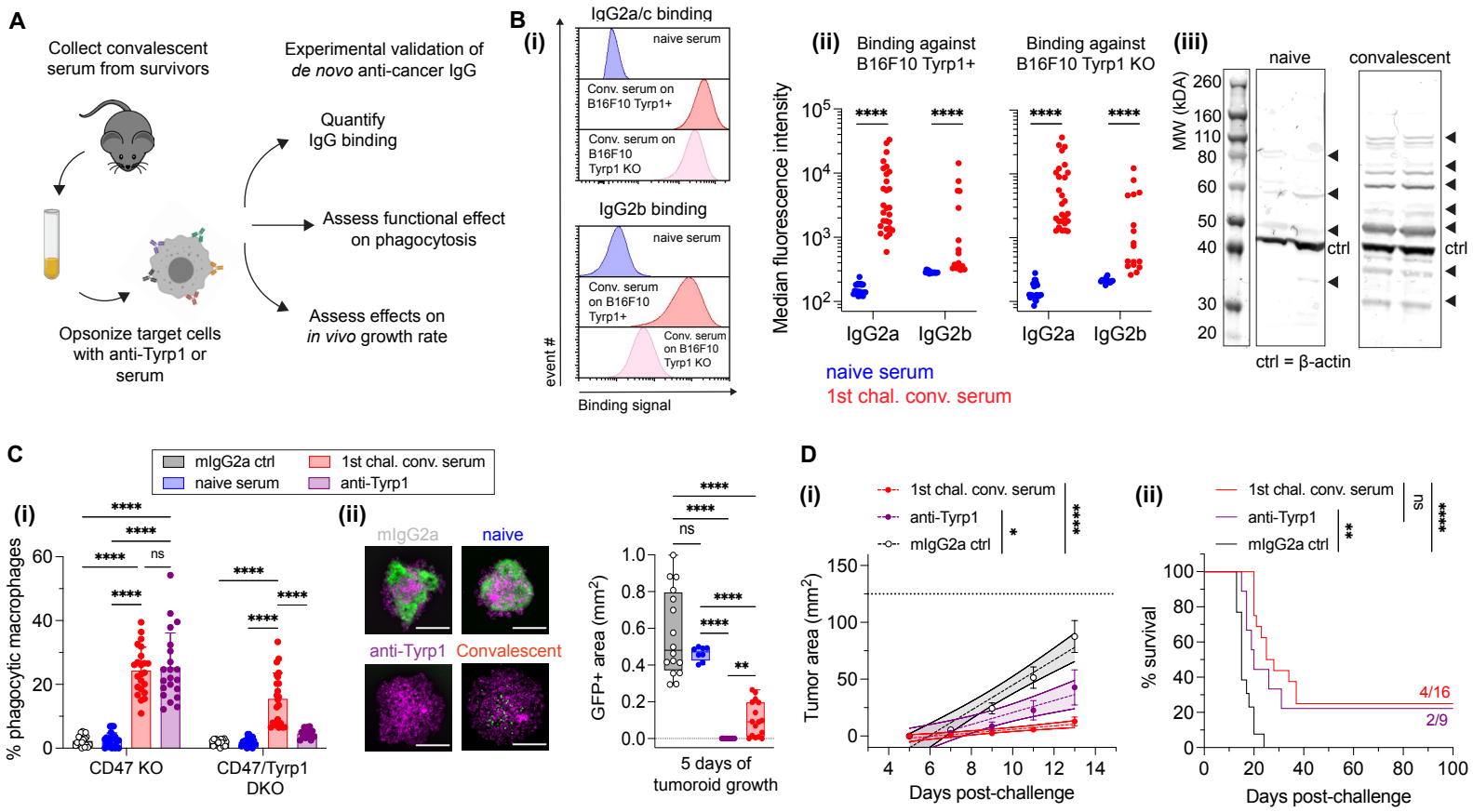

Rechallenges on survivors further shows acquired immunity & immune response against both genomically stable and unstable tumors

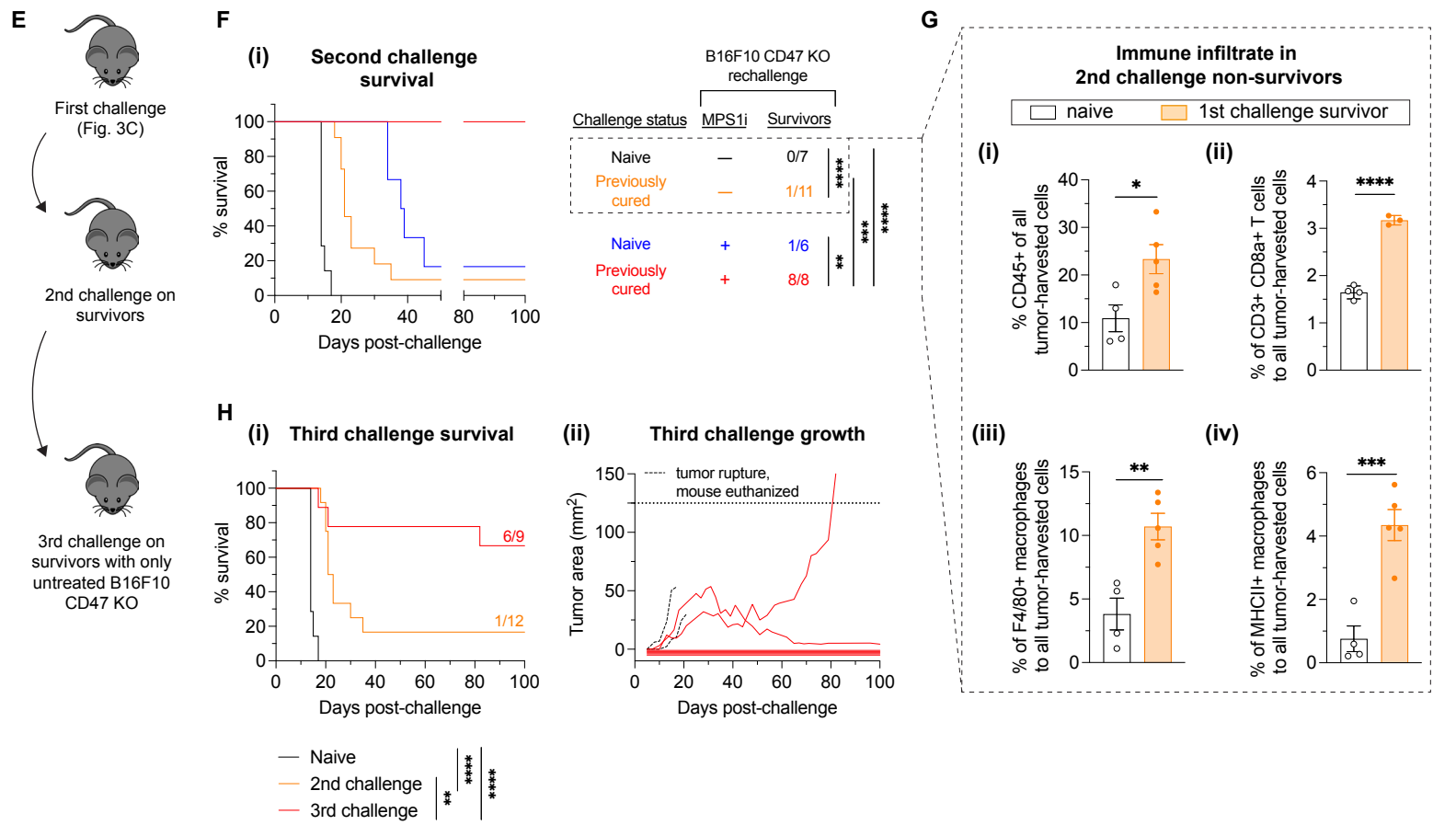

Supplementary Figure 1

Induction of micronuclei and chromosomal instability in B16F10 by MPS1i

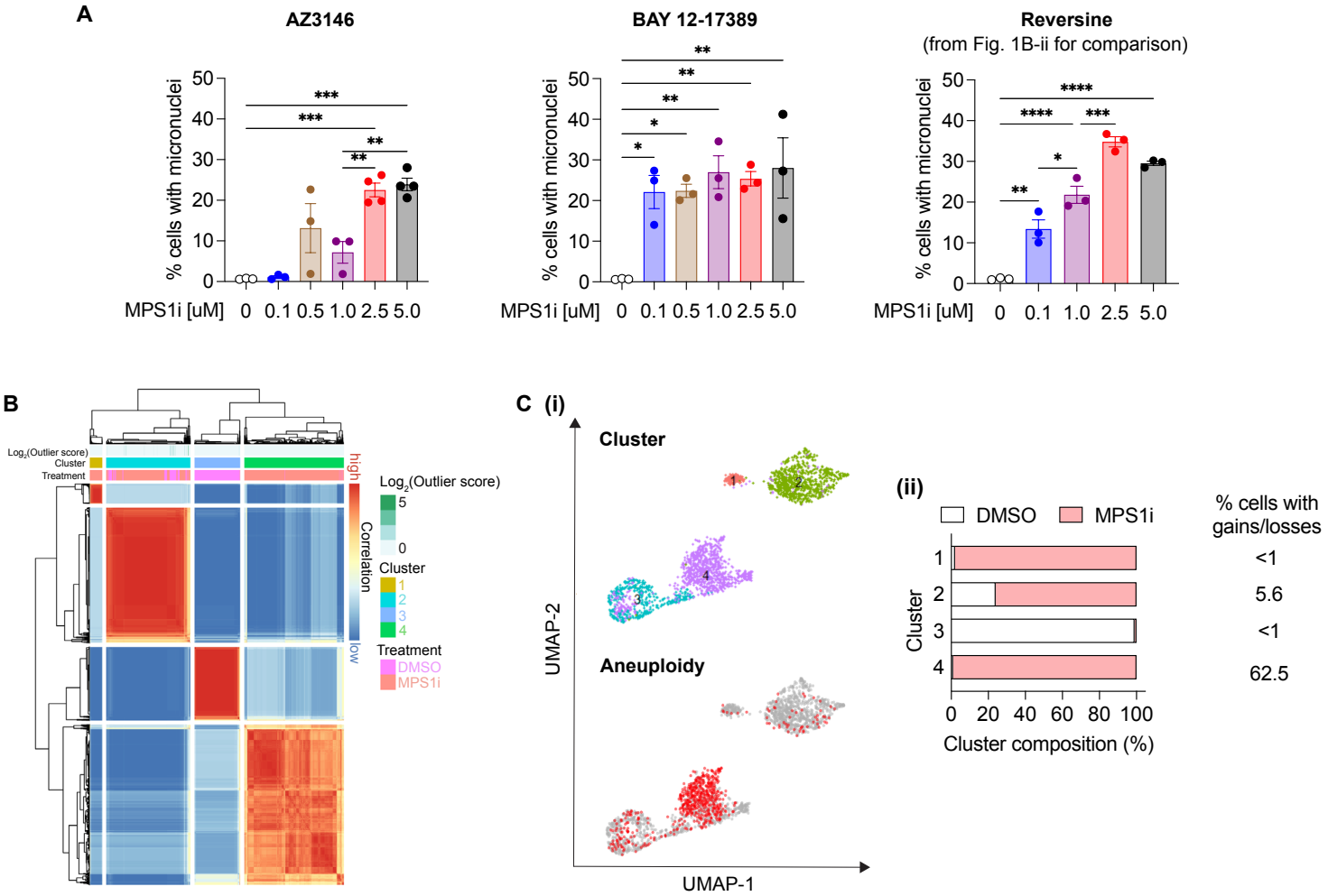

Supplementary Figure 2

Characterization & validation of factors affecting phagocytosis

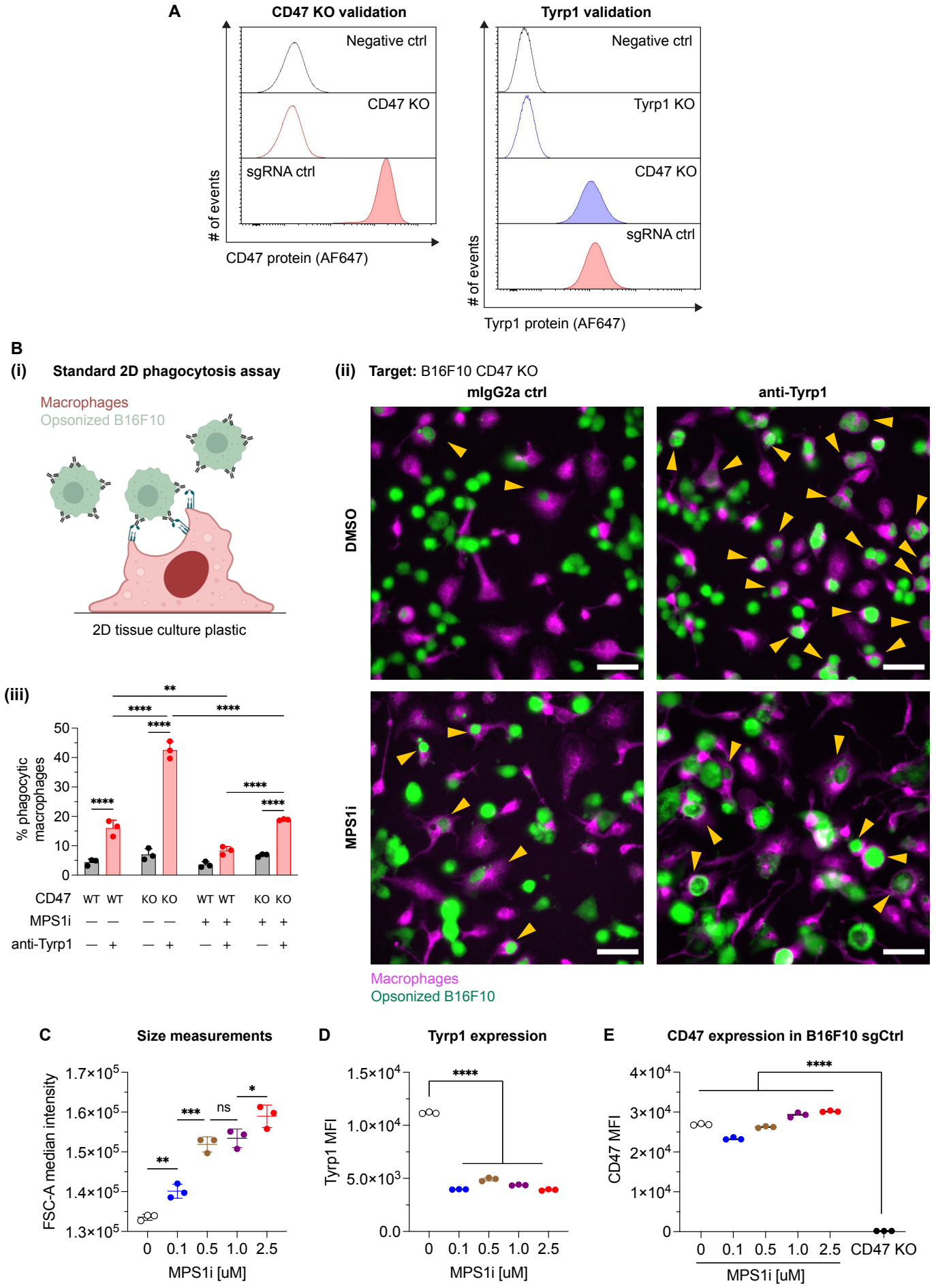

Supplementary Figure 3

MPS1i-induced CIN favors clearance with CD47 ablation and IgG opsonization, regardless of MPS1i concentrtion

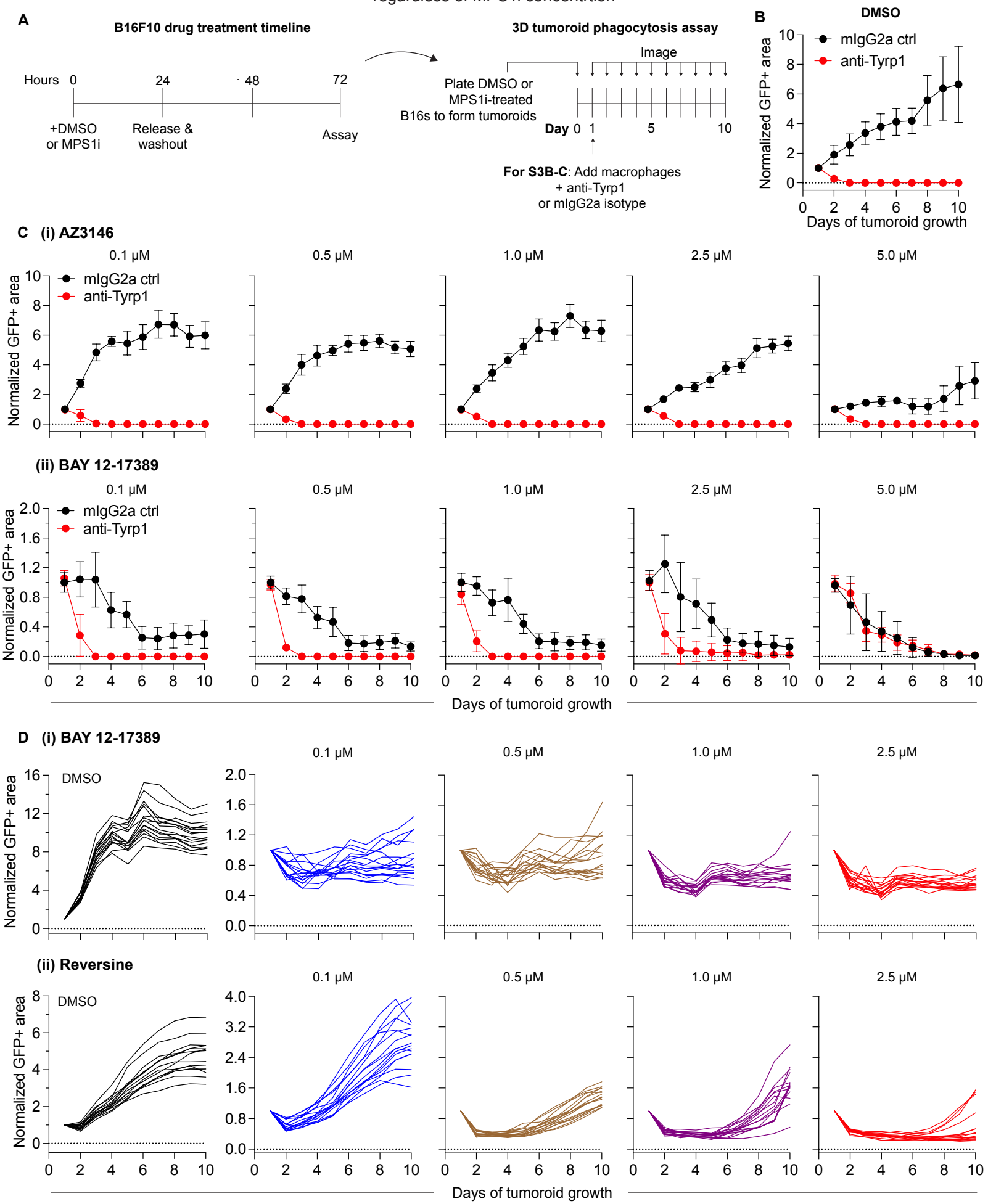

Supplementary Figure 4

MPS1i also induces upregulation of MHC-I class molecules

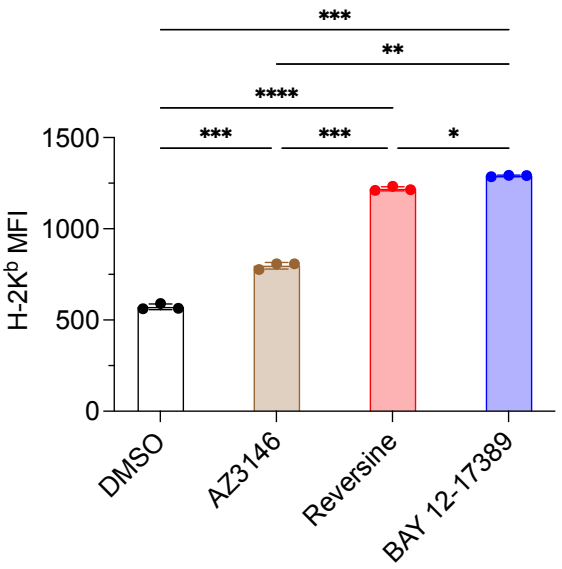

Supplementary Figure 5

Immune infiltrate analysis in MPS1-treated and DMSO-treated tumors

A **Chromosomally stable tumor (DMSO-treated B16F10)**

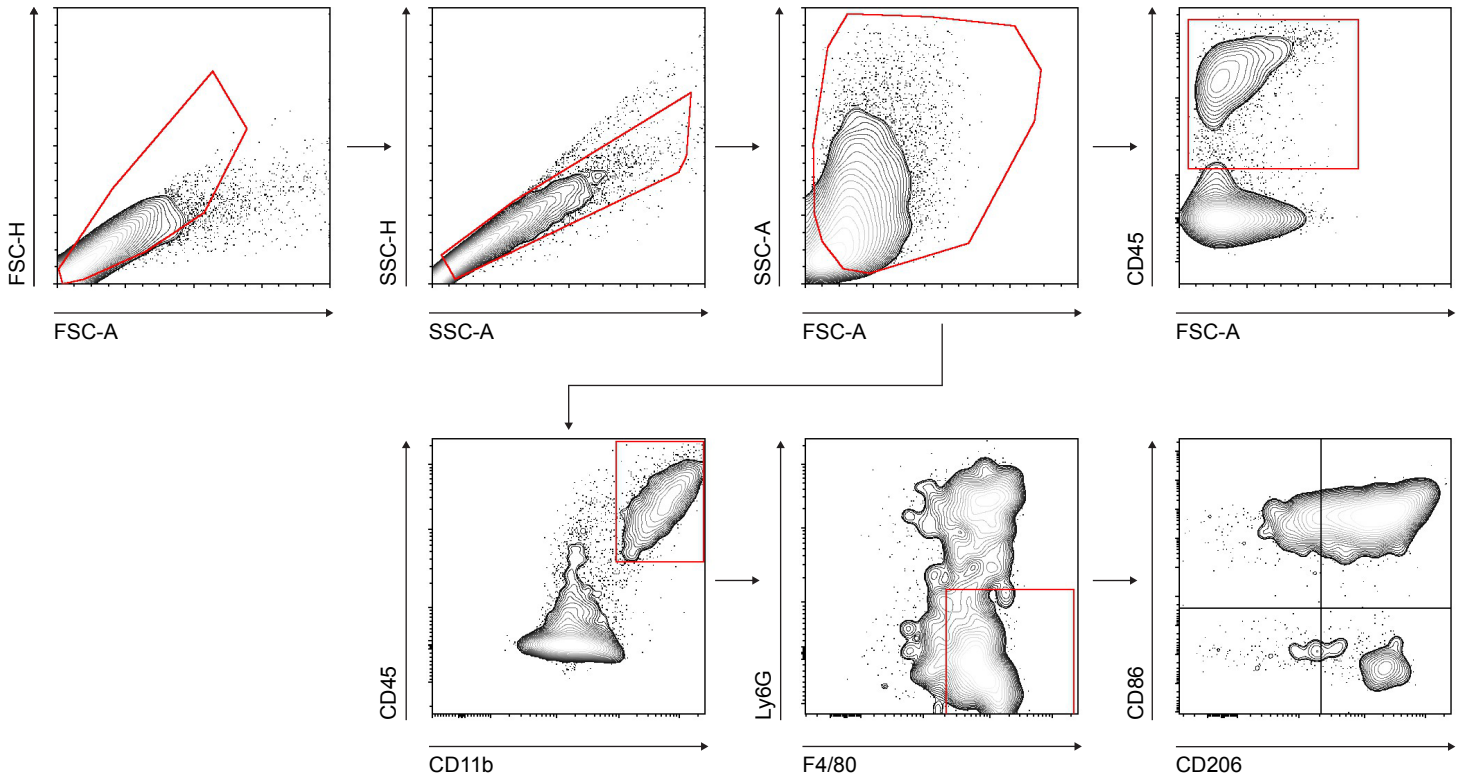

B **Chromosomally unstable tumor (MPS1i-treated B16F10)**

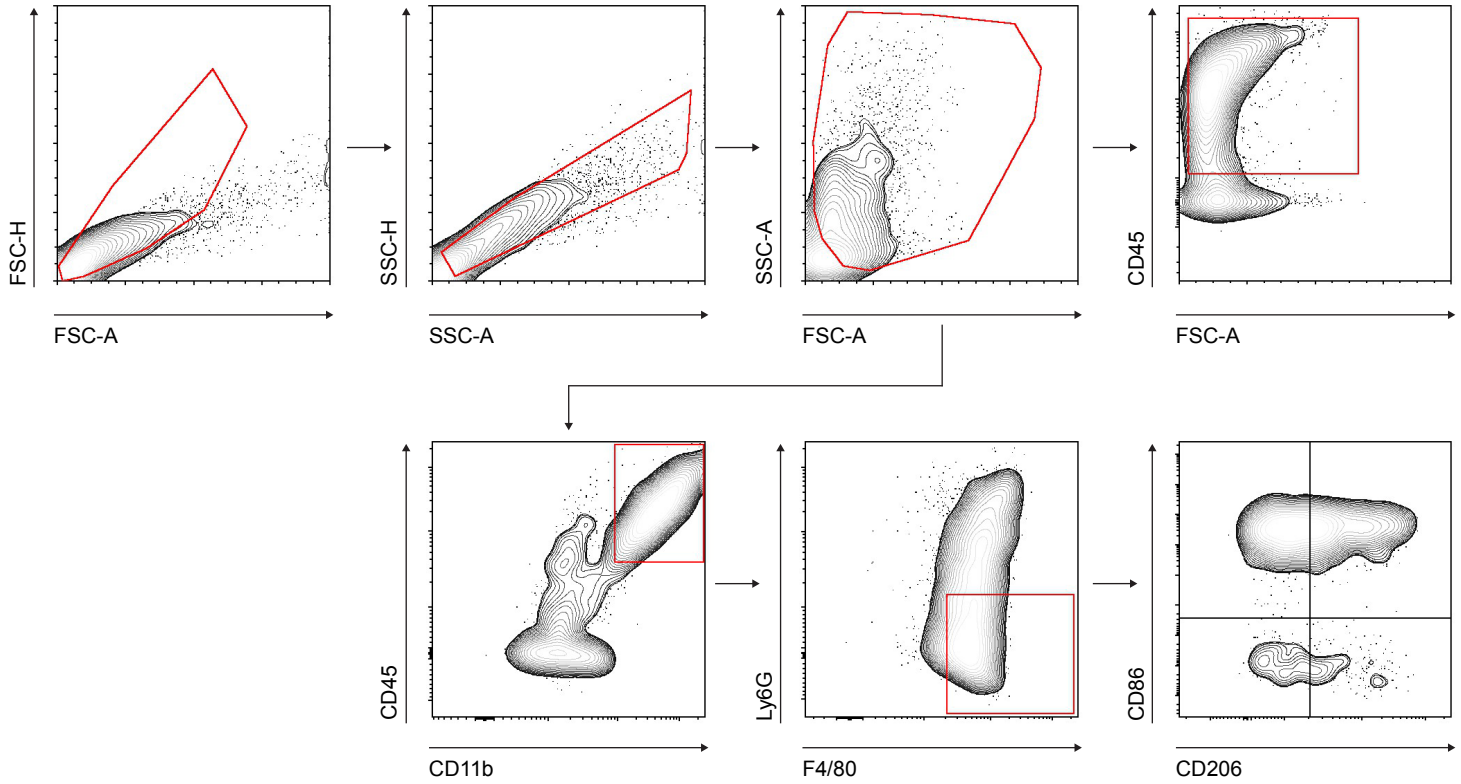

Supplementary Figure 6

MPS1i-induced CIN favors *in vivo* clearance with CD47 ablation and IgG opsonization, regardless of degree of CIN

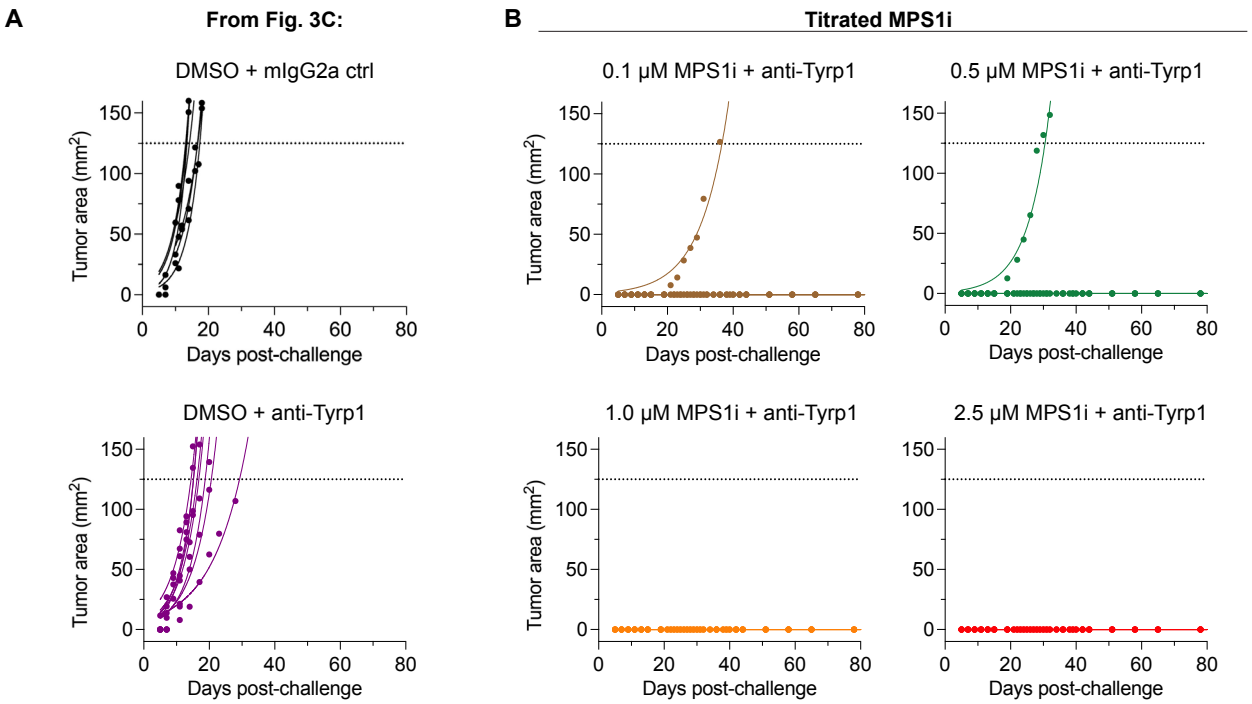

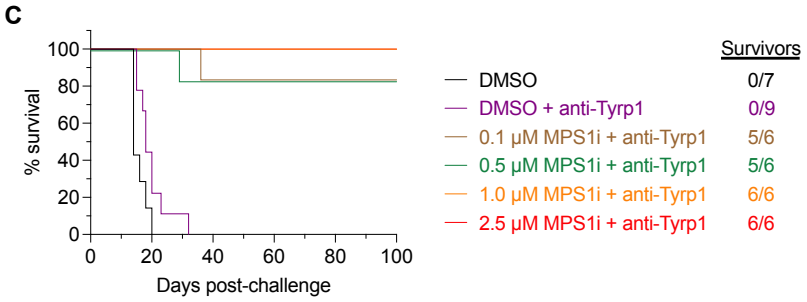

Supplementary Figure 7

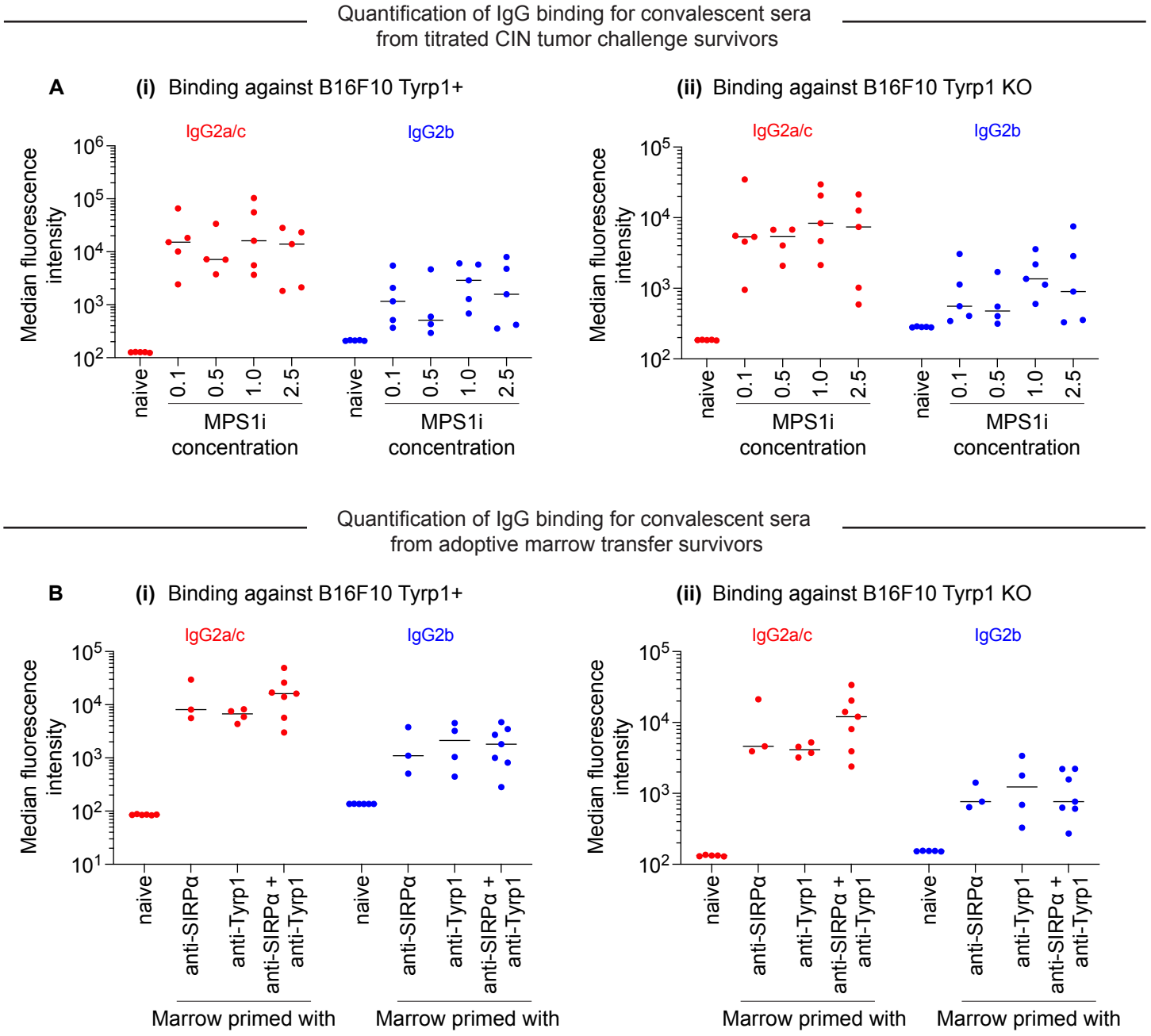
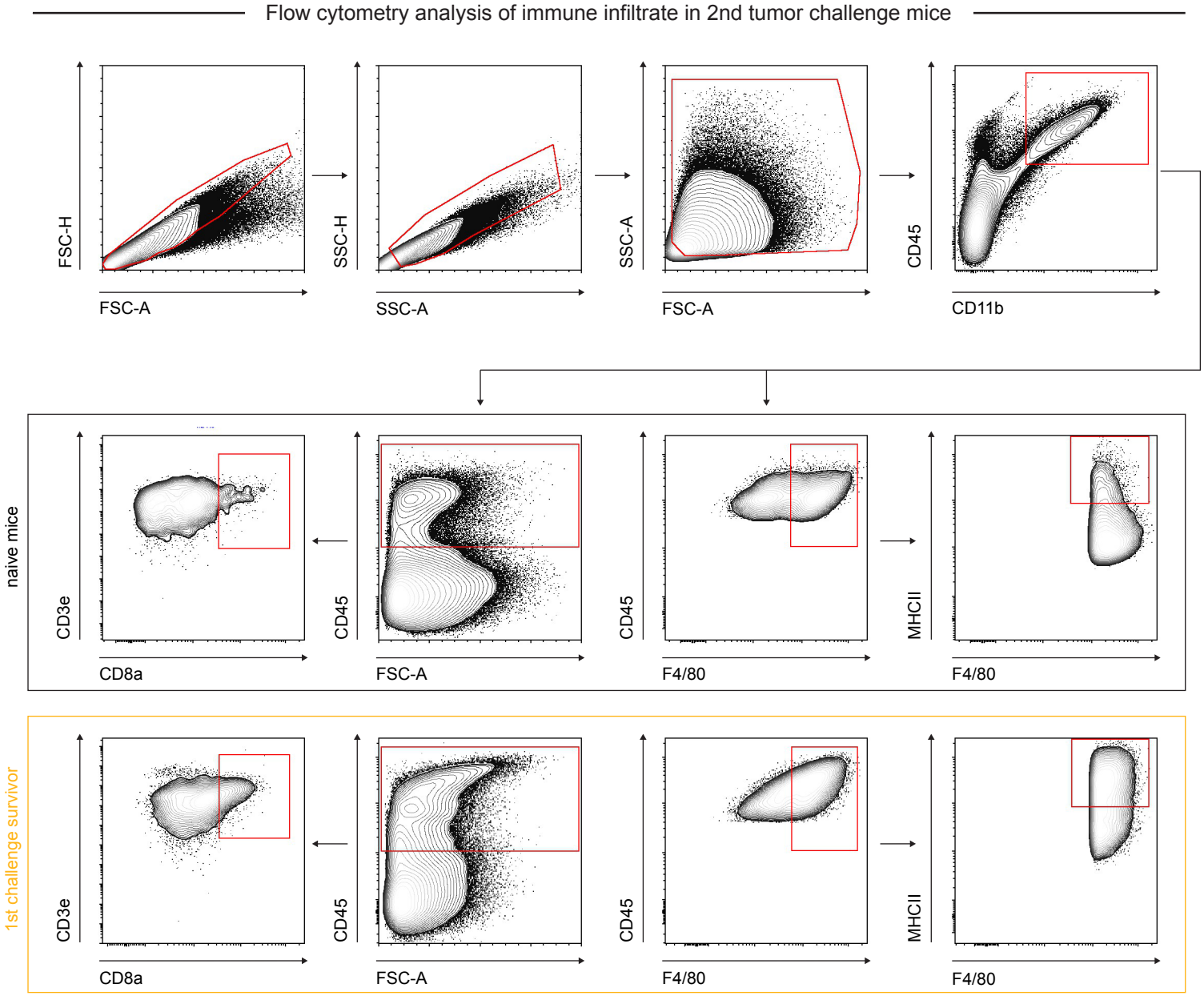
Supplementary Figure 8